Journal Pre-proof

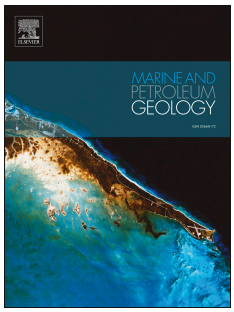

The Paleocene Hangu formation: A key to unlocking the mysteries of Paleo-Tethys tectonism

Ahmer Bilal, Renchao Yang, Nils Lenhardt, Zuozhen Han, Xiwu Luan

PII: S0264-8172(23)00414-2

DOI: https://doi.org/10.1016/j.marpetgeo.2023.106508

Reference: JMPG 106508

To appear in: *Marine and Petroleum Geology*

Received Date: 10 July 2023

Revised Date: 15 September 2023

Accepted Date: 17 September 2023

Please cite this article as: Bilal, A., Yang, R., Lenhardt, N., Han, Z., Luan, X., The Paleocene Hangu formation: A key to unlocking the mysteries of Paleo-Tethys tectonism, *Marine and Petroleum Geology* (2023), doi: https://doi.org/10.1016/j.marpetgeo.2023.106508.

Graphical Abstract

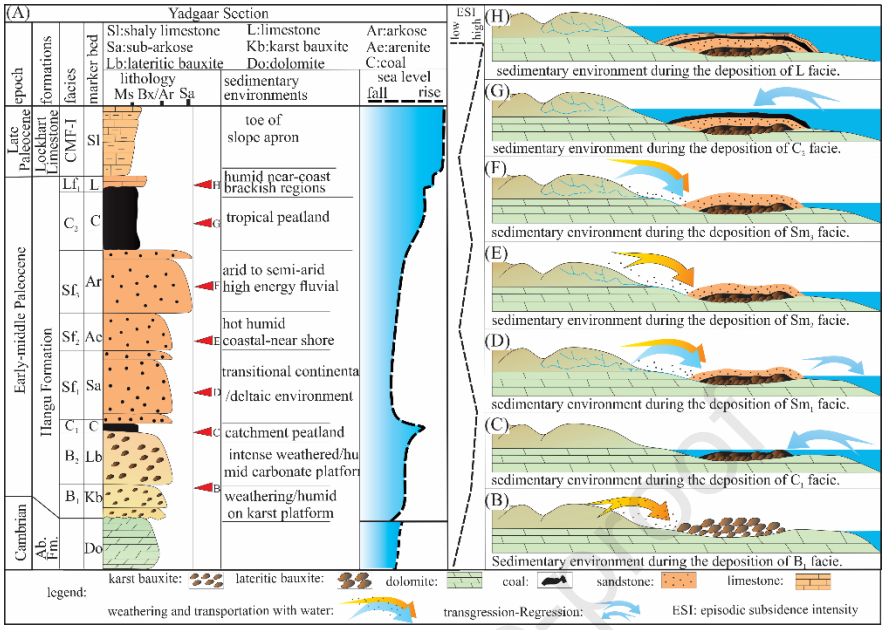

The Paleocene Hangu Formation: A Key to Unlocking the Mysteries of Paleo-Tethys Tectonism

Ahmer Bilal[1], Renchao Yang[1,2]*, Nils Lenhardt[3], Zuozhen Han[1], Xiwu Luan[1]

[1] Shandong Provincial Key Laboratory of Depositional Mineralization & Sedimentary Minerals, Shandong University of Science and Technology, Qingdao 266590, China, ahmerbilal@126.com

[2] Laboratory for Marine Mineral Resources, Qingdao National Laboratory for Marine Science and Technology, Qingdao 266071, China

[3] Department of Geology, University of Pretoria, Private Bag X20, 0028 Pretoria, South Africa

Original Article

* Corresponding author. E-mail: yang100808@126.com

ABSTRACT

The sedimentary rocks of the Paleocene Hangu Formation in the Yadgaar Section of the Upper Indus Basin in northern Pakistan, have been the subject of an integrated field, petrographical, and sedimentological investigation. The goals of this study are to improve our understanding of the sedimentary environment, facies shifts, and the impact of tectonism on the genesis of the investigated sedimentary facies. A better understanding of the intricate relationships between the aforementioned factors will clarify whether the regional tectonic drive has partial control over or complete command of the sedimentation processes. The results of this study shows that the Hangu Formation consists of four facies: bauxite, sandstone, coal, and limestone. The bauxite deposits formed in a karst environment with severe chemical weathering in a humid to extremely humid climatic setting. Thin coal laminae indicate a peatland environment that formed within a humid tropical climate. Sub-arkose, arenite, and arkose sandstone facies mark deltaic (sub-humid), coastal–near shore (humid to hot-humid), and high-energy fluvial (arid to semi-arid) sedimentary environments, respectively. Finally, the occurrence of marly limestone points towards deposition on a shallow marine carbonate platform within a coastal-brackish environment. The facies shift of the sediments provides evidence for a gradual transition from continental to marine conditions within the study area, together with episodic transgressive and regressive cycles as well as changing climatic and geomorphological conditions. In consequence, all these changes are controlled and shaped by the effects of Paleo-Tethys tectonism during the Indo-Eurasian intra-oceanic subduction. This advancement through the current work helps in understanding tectonic-sedimentary mechanics, i.e., how regional tectono-sedimentological processes influence the formation of sedimentary sequences.

Keywords: Facies shift; Lithofacies; Hangu Formation; regional tectonism; sedimentology; sedimentary environment

1. Introduction

The association of karst features with lateritic bauxite indicates an intricate geological history that includes multiple stages of weathering, erosion, and deposition (Gu et al., 2013) and reveals much about the paleoenvironment and paleoclimate in which both formed (Fig. 1). Karst landscapes develop in humid, water-rich climates due to the extensive dissolution of soluble carbonate rock by meteoric or groundwater (Kiaeshkevarian et al., 2020; Kelemen et al., 2022). In contrast, the genesis of bauxite, the world's main source of aluminum, indicates intense weathering of aluminosilicate-rich precursor rocks (such as basalt, etc.) in a tropical climate. Bauxite, a mixture of residual deposits of Fe-oxy-hydroxides, Ti-oxide, kaolinite, and Al-hydroxides, can be further subdivided into karst bauxite, sedimentary bauxite, and lateritic bauxite (Meyer, 2004; Sun et al., 2020).

Lateralization, or tropical weathering, of *in situ* aluminosilicates results in the formation of lateritic bauxite. Surficial sedimentary processes may rework these lateritic bauxite deposits into sedimentary bauxites, which are essentially the products of proximal redeposition (Bogatyrev et al., 2009). Lateritic bauxite is economically the most important type of bauxite, providing >90% of the world’s bauxite resources (Fig. 1) (Nurhawaisyah et al., 2021). A karst bauxite profile commonly differs from a laterite profile. However, evidence for a protolithic carbonate rock is frequently eroded (Boni et al., 2013; Mondillo et al., 2021), and finding a carbonate bedrock at the base of a karst bauxite deposit is extremely rare. Furthermore, karst bauxite had previously been reported only from Paleozoic-Mesozoic rocks in the northern hemisphere and had not been found

in Cenozoic rocks in the equatorial regions (Fig. 1) (Mondillo et al., 2021). A carbonate platform near the continental margin is an ideal environment for karst bauxite formation. Karstification of these deposits may result from deep weathering and Al-rich solution filling of carbonate and preexisting laterite (Combes, 1990; Basilone et al., 2017).

Since bauxite forms during long periods of intense weathering, its presence within a stratigraphic sequence frequently indicates an unconformity, i.e., a period of weathering, erosion, and non-deposition. Bauxite deposits are typically associated with tectonic uplift. As a result of tectonic uplift, the precursor rock is exposed to the tropical climate, resulting in intense physical and chemical weathering. The weathered aluminum and iron mineral components may then be transported by gravity or water and eventually be deposited in low-gradient areas such as river valleys and coastal plains (Guyonnet-Benaize et al., 2010). As a result, the age of bauxite can reveal details about the tectonic history and paleoclimatic conditions of a region. Furthermore, bauxite deposits offer a potential target for the mining industry.

[Fig. 1 about here.]

Fig. 1. Global distribution of karst and lateritic bauxite and the location of the study region (modified after (Schulte and Foley, 2014).

In the eastern margin of the Upper Indus Basin (UIB; Pakistan; Fig. 2A), the so-called Yadgaar Section was studied in the core of the Hazara Kashmir Syntaxis (HKS) (Fig. 2B) (Critelli et al., 1990; Critelli and Ingersoll, 1994; Bilal et al., 2022a). The Yadgaar Section consists of the Hangu Formation, which incorporates bauxite deposits and associated sandstone, coal, and limestone deposits (Fig. 3). The Cambrian dolomite of the Abbottabad Formation marks the unconformable

lower contact, while the conformable upper contact of the Hangu Formation is marked by the shale and limestone of the Lockhart Limestone (Fig. 3). The interaction and transition of the different facies within the Hangu Formation may aid in interpreting the underlying paleoenvironmental and paleoclimatic conditions. A facies shift from a continental to a marine environment may be related to tectonic activities such as subsidence (Amorosi et al., 1999). It may further indicate supply variations of sedimentary influx, changing climatic conditions, and the existence of transgression-regression cycles with or without active tectonism (McGowran, 2009; Hoentzsch et al., 2013). A careful consideration of all these factors before interpretations can help improve the accuracy of discussions of the sedimentary environments and facies shift. In particular, just before the Paleocene–Eocene Thermal Maximum (PETM; in the early Eocene), a continental-marine facies shift is known from the Indian continental margin (Li et al., 2022), which is characterized by the deposition of a mixed carbonate-siliciclastic rock sequence during the Eocene (Malekzadeh et al., 2020; Al-Rajhi et al., 2021).

[Fig. 2 about here.]

Fig. 2. (A) A regional tectonic model and the location of the study area; (B) the tectono-sedimentary setting of the Hazara Kashmir Syntaxis (HKS) (modified after (Bilal et al., 2022c).

Previous researchers only conducted low-resolution investigations on the Hangu Formation and focused on very selective targets (Warwick et al., 1995; Munir et al., 2006; Baig and Munir, 2007). Few authors have made an effort in the past to develop a general study on the stratigraphy, metamorphism, deformation, and economic significance of coeval rocks in the surrounding areas (Calkins and Matin, 1973; Chakrabarti, 2016; Ullah et al., 2018; Khan et al., 2022a). However, a

comprehensive sedimentological study using modern techniques and tools that describes the sequential shift of conditions from continental to marine and the respective deposition of the strata is still missing in the study area. A study focusing on petrography, sedimentology, and paleoclimate could thus provide new, much-awaited tectono-sedimentological information. Therefore, this contribution aims to provide new information on the paleo-tectonic setting, the sedimentary environment, and shifts therein of the Hangu Formation and their relationship to the Cenozoic evolution of the Neo-Tethyan Ocean (Critelli and Martín-Martín, 2022; Jafarzadeh M et al., 2022; Martín-Martín et al., 2023). The work to achieve these goals includes integrated field work and petrological analysis of the Yadgaar Section's bauxite and associated sandstone, limestone, and coal deposits. The results of this contribution are expected to reveal the dynamics of continental–marine facies transitions in such a way that their interpretations, including their economic merits, paleoenvironmental and paleoclimatic reconstructions. Moreover, the information on transgression-regression cycles, may be used as general standards that may help us to understand to what degree regional tectonics have control over the climate, the role of climatic conditions in defining the character of sedimentary facies, and the effect of regional tectonics on the sedimentary facies shift through the shaping of the sedimentary basin.

2. Geological setting

The Indus Basin (IB) of Pakistan is subdivided into upper, central, and southern subbasins by a series of NW-trending basement highs (Kadri, 1995). The IB consists of Precambrian to recent thick sedimentary sequences (Shah, 2009) above the Archean crystalline basement. These geological strata are significant because of the economic components they contain, such as gas (Craig et al., 2018), oil (Awan et al., 2021), bauxite/laterite, uranium, copper, and other important

metal deposits (Malkani et al., 2016). The UIB is located in the north of Pakistan and close to the adjacent Himalayas (Craig et al., 2018).

2.1. Geological development of the Indus Basin

In contrast to the Southern Indus Basin (SIB), where marine sedimentation occurred between the Mesozoic and Cenozoic (with a few Late Paleogene to Neogene exceptions), the UIB is defined by a 13-16 km-thick sequence that spans the Precambrian to the Holocene (Figure 3; (Afzal et al., 2009)). The basement is made up of Proterozoic igneous and metamorphic rocks that are part of the Indian Shield (Khan et al., 2022b). These Precambrian rocks are unconformably overlain by Paleozoic clastic and non-clastic sedimentary sequences of the UIB that are delineated by the Khewra Trap in the Salt Range and the Tanaki basal conglomerate in the Hazara regions (Gaetani et al., 2004; Khan et al., 2022b).

During the Paleozoic, sedimentary, metasedimentary, and metamorphic rocks formed in the UIB. Sandstones, mudrocks, fossiliferous limestones, and minor dolostones were deposited under deltaic conditions during this time (Yaseen et al., 2021). The Paleozoic rocks are further para-conformably overlain by Mesozoic non-clastic and clastic marine sequences. During Triassic and Jurassic times, the UIB was characterized by deposition on a continental shelf (Shah, 2009). The platform sediments are well-developed, comprising limestones and dolostones with a high abundance of fossils. During the late Jurassic, there was an increase in ferruginous material, shale, and sandstone, suggesting the start of a regression phase in the basin. Together with the fall in sea level, a facies shift from marine to terrestrial conditions can be deduced (Malkani et al., 2016).

From the Late Jurassic to the Cretaceous, sedimentation conditions remained largely constant (Khan et al., 2022b). The southern part of the UIB was characterized by sedimentation of carbonate rocks in a shelf environment, whereas the central and northern parts had already experienced

clastic and minor volcanic rock input, indicating terrestrial conditions (Shah, 2009; Chaudhuri et al., 2018; Chaudhuri et al., 2023). The Cretaceous sediments can be found broadly throughout the IB (DeCelles et al., 2014). The Paleogene was marked by a transition from continental to marine sequences, followed by a return to continental facies (Bilal et al., 2022a; Bilal et al., 2022b; Bilal et al., 2022c). This sequence is overlain by Neogene and Quaternary clastic molasse sediments and conglomerates (Mughal et al., 2018; Zaheer et al., 2022).

2.2. Stratigraphy of the study area

The study area is located in the northeastern corner of the UIB. Here, the Precambrian metasediments of the Hazara Formation indicate deep marine deposition of turbidites (Dar et al., 2021). These rocks are overlain by the Abbottabad Formation, a Cambrian-aged cryptocrystalline-algal dolostone that suggests a shallow subtidal to supratidal environment (Qasim et al., 2014). A large unconformity encompasses the entire time from the Ordovician to the late Cretaceous (Bilal et al., 2023), after which the Hangu Formation, representing renewed Paleocene sedimentation, can be found. The sediments of the Hangu Formation comprise bauxite, sandstones, limestones, and two coal seams below and on top of the sandstone (Munir et al., 2006). The Hangu Formation is the economically richest and most important unit in the IB. At least one recent study describes the bituminous coal within the formation (Qureshi et al., 2020). In a few areas, the shale of the Hangu Formation shows high potential as a source rock for both oil and gas in the IB (Khan et al., 2022a). Shales were not encountered in the outcrops of the study area, though. This may be due to the presence of formation in a highly fractured zone, which may have displaced or eroded the shale from the outcrop.

Regional coeval rocks are highly valuable in terms of their coal and hydrocarbon source potential (Calkins and Matin, 1973; Hakimi et al., 2013; Abbassi et al., 2016; Escobar et al., 2016;

Friederich et al., 2016; Khan et al., 2022a). So far, within the study area, the Hangu Formation has only been studied for biostratigraphy and its engineering properties and has not been evaluated thoroughly (Munir et al., 2006; Basharat et al., 2020). The regional importance of the Hangu Formation and the lack of sedimentological and petrological evaluation make this formation a perfect candidate for a detailed study. The Hangu Formation in the Yadgaar Section is overlain by thick Paleogene carbonate strata with a few clastic units representing a shallow shelf to deep marine sedimentary environment (Bilal et al., 2022a; Bilal et al., 2022b; Bilal et al., 2022c; Bilal et al., 2023). Above these Paleogene deposits, thick strata of sandstone and shale from the early Neogene Murree Formation blanket the older rocks in the area (Critelli and Garzanti, 1994; Mughal et al., 2018).

2.3. Tectonic setting

The IB lies on the north-west part of the Indian Plate (Bilal et al., 2022b). The basin experienced a history of tectonic events, due to which the basin shape experienced a morphological evolution (Kazmi and Jan, 1997). Due to this, the basin's present shape subdivides the basin into further sub-basins. The northern sub-basin is also known as the UIB (Kadri, 1995). The boundaries of the UIB are marked by the Main Boundary Thrust (MBT) toward the north and east (Shah, 2009; Ehsan et al., 2021). In the south and west, several highs and the Kurram Thrust delineate the brinks (Badshah et al., 2000).

During the Early Paleozoic, the Indian Plate formed part of Gondwana. During its northern drift, the plate experienced several tectonic events, such as rifting and uplift (Wang et al., 2021). The appearance of conglomerates during the Late Cretaceous reflects the presence of the Kohistan Island Arc (KIA) in the north of the basin, which came into being by an intra-oceanic subduction between the Indian and Eurasian plates during the Mesozoic era (Wang et al., 2015; Ullah et al.,

2020a; Hameed et al., 2023). This oceanic arc (KIA) collided with the Indian Plate during the early Cenozoic at around 60 Ma (Chatterjee and Bajpai, 2016). The Tethys Trench between India and Eurasia continued to exist until close to the Paleocene/Eocene boundary, i.e., until the Indo-Eurasian collision and the thrusting and active uplifting of the Himalayas (Critelli et al., 1990; Critelli and Ingersoll, 1994; Ullah et al., 2020b; Hameed et al., 2023).

During this long-time drift from Gondwana towards the north and until the beginning of the Himalayan Orogeny, the Indian Plate experienced multiple events of rifting, uplifting, weathering, and erosion (Chatterjee and Bajpai, 2016; Wang et al., 2021; Hameed et al., 2023). This resulted in the formation of several unconformities and related strata in the IB (Shah, 2009). The intense erosional events of the Mesozoic rocks led to the formation of the Paleocene sedimentary sequence of the Hangu Formation in the Yadgaar Section.

[Fig. 3 about here.]

Fig. 3. (A) The lithology, sedimentary environments, and facies of the Yadgaar Section.

3. Data and methods

3.1. Field study

The study area is located in Pakistan's Yadgaar Section, between Ghori-Patika village and Muzaffarabad city. The fieldwork comprised the description of the Hangu Formation and its relationship to the surrounding formations toward the top and the base. In outcrop, hand-specimen, and thin-section scales, a detailed facies analysis, including a textural study, was performed. For petrographic studies, fresh representative samples of bauxite, sandstone, and limestone were

collected. Thin-section preparation was carried out at the Institute of Geology, University of Azad Jammu and Kashmir (UAJ & K), Muzaffarabad, Pakistan.

3.2. Petrographical study

A petrographical study was carried out in the mineralogy/petrology laboratory of the UAJ & K. A polarizing microscope (Leica-DM 750P) and a stereo zoom microscope (Leica-S6D) (both from Leica Microsystems Ltd., Heerbrugg, Switzerland) were used to identify and record photomicrographs of the microfossils, calculate the modal mineralogy, and differentiate the different facies types in thin sections. A Leica-EC3 camera was used to take photomicrographs. A climate diagram was used to deduce paleoclimatic conditions (Suttner and Dutta, 1986). The sandstone composition was quantified according to (Folk, 1968).

4. Results

4.1. Field study

The rocks of the Hangu Formation consist of bauxite, coal seams, sandstone, and limestone (Fig. 4A). The Yadgaar Section starts with ca. 1.7 m of bauxite. The color of this facies is dark gray to black in outcrop (Fig. 4B). An approximately 8 cm-thin black-colored coal seam is present above the bauxite (Fig. 4C). After this coal seam, a few beds of ferruginous sandstone (from 15 to 300 cm in thickness) can be identified. The sandstone is fractured and displays blocky cracks in the outcrop (Fig. 4D). Limonite with a green color can be observed in some places near the base of the sandstone (Fig. 4C). The fresh color of the sandstone is light gray, whereas the weathered color is golden brown to dark brown in the outcrop (Figs. 4E–F and 5A–B). From the base toward the top, a gradual increase in bed size can be observed within the studied section (Fig. 3).

[Fig. 4 about here.]

Fig. 4. Field images of the Hangu Formation facies suit. (A) the unconformable lower contact with Abbottabad Formation (Ab. Fm.: Abbottabad Formation; B_1: Bauxite layer 1; B_2: Bauxite layer 2; C_1: Coal layer 1; Sf_1: Sandstone facies 1); (B) bauxite and coal strata; (C) limonite from the sandstone leaching onto the lower coal deposit; (D) sub-Arkose sandstone beds; (E) and (F) coarse-graines sub-arkose sandstone (length of the blue cap of the pen is 2.5 cm). For abbreviations, please see Fig. 3.

Above the sandstone facies, another thick coal seam (ca. 2 m) appears. This coal seam is mainly mined and excavated from the type section, and only remnants can be observed (Fig. 5C). The top strata of the Hangu Formation consist of gray to dark brown micritic marly limestone near the upper contact (Figs. 5D and 5E). The thickness of this facies is ca. 40 cm in the studied section. The upper contact with the overlying Lockhart Limestone is rarely exposed due to dense vegetation and debris resulting from the mining activity in the Yadgaar Section. However, petrographic studies have shown that the lower part of the Lockhart Limestone is characterized by a micrite-dominated mudstone-wackestone (Fig. 5F) (Bilal et al., 2022b).

[Fig. 5 about here.]

Fig. 5. Field images of the Hangu Formation facies suit. (A) arenite facies; (B) arkose facies; (C) coal facies; (D) framboidal pyrite transitioning into hematite, which further replaces bioclasts in the micrite matrix (PPL); (E) limestone facies with upper contact to the overlying Lockhart Limestone; (F) green algae fossils that are partially micritized due to diagenesis (Bilal et al., 2022b) (PPL).

4.2. Petrography of the Hangu Formation bauxite

In the Yadgaar Section, the bauxite deposits display angular and brittle deformation. Petrographic data from six samples throughout the bauxite deposit reveal that hematite, in the form of cement and veins, is the dominant mineral (47% on average; Fig. 6A) in the studied thin sections (Table 1). Diaspore can also be identified within the thin sections (Fig. 6A). The mineral shows a decreasing trend from the base to the center of the bauxite section, while it is absent at the top (Table 1). Diaspore is present with an average of 10% in the bauxite thin sections. After this, kaolinite can be observed (Fig. 6B). The kaolinite percentage shows a gradually increasing trend while moving from the base towards the top. Kaolinite is present in thin sections with an average of 19% (Table 1). Quartz is highly fractured, with the fractures being filled with hematite cement (Figs. 6B and 6C). Moving toward the middle samples of the bauxite deposit, gibbsite starts to appear in thin sections (Fig. 6D). Kaolinite and hematite also start to increase in percentage with the appearance of hematite veins (Fig. 6E and 6F).

[Fig. 6 about here.]

Fig. 6. Photomicrographs of the karst bauxite thin sections of (HB1– HB3): (A) diaspore and hematite (X-PL); (B) fractured quartz, hematite, and kaolinite (X-PL); (C) fractured quartz with fractures filled with hematite cement (X-PL); (D) gibbsite grains (PPL); (E) kaolinite and hematite (X-PL); (F) older hematite veins are cut by younger kaolinite veins (X-PL). The arrows denote the following minerals: dark blue: diaspore; brown: hematite; green: fracture quartzite; sky blue: kaolinite; sky blue arrows with red outline: kaolinite vein; red: gibbsite; brown arrows with red outlines: hematite veins.

Gibbsite (aluminum hydroxide) is a secondary mineral that forms as a result of the weathering of alumino-silicate minerals. In the studied thin sections, it is the second most abundant mineral (22% on average; Table 1), with an increasing trend from the base to the top of the bauxite deposit (Fig. 7A and B). Lateritic circular hematite and goethite veins can also be observed only in the top portion of the bauxite (Fig. 7C and D). Furthermore, a high amount of kaolinite and few limestone clasts can be observed (Fig. 7E and F).

[Fig. 7 about here.]

Fig. 7. Photomicrographs of the lateritic bauxite thin sections of (HB4–HB6): (A-B) gibbsite grains (PPL); (C) lateritic circular hematite and kaolinite (X-PL); (D) goethite veins (X-PL); (E) hematite and kaolinite (X-PL); (F) gibbsite, hematite, and limestone clasts (X-PL). The arrows denote the following minerals: brown arrows with yellow outlines: lateritic circular hematite; purple: goethite; purple arrows with green outlines: goethite veins; yellow: limestone clasts. See figure caption of Fig. 3 for additional arrow colors.

Table 1 Mineralogical composition of studied bauxite deposits. The minerals are sorted according to their economic value. Sample numbers HB1–2 represent karst, while HB3–6 represent lateritic bauxite.

[Table 1 about here.]

4.3. Integrated facies assessment of the Hangu Formation sandstone

All sandstone samples of the Hangu Formation are matrix-free. While moving up section through the sandstone, the samples show a predominance of non-undulatory monocrystalline quartz. These monocrystalline quartz grains are more abundant in samples from the center of the sandstone, and from there they decrease towards the top (Table 2).

The samples from the top of the sandstone show almost an equal amount of monocrystalline and polycrystalline quartz. Feldspar grains such as plagioclase and perthite can also be observed in the samples from the base and top of the section. However, these feldspar grains were found to be absent in the samples collected from the center (Table 2). Orthoclase grains are consistently found throughout the section. However, they are observed with a decreasing trend from the sample at the base to those in the center, while an abrupt increase in percentage can be noted in the samples at the top. Rock fragments are rarely found in the samples of the Hangu Formation.

Accessory minerals such as tourmaline, sericite, and zircon are found in trace amounts throughout the formation. Rutile grains are rarely found in the samples from the base and near the top of the section. Muscovite, biotite, chlorite, calcite, and pyrite grains are also found in minor amounts in the samples from the middle and the top. Small amounts of hematite grains have been found in samples near the top of the Hangu Formation's sandstone. Silica is the dominant cementing material in the sandstone samples. The lower to middle part of the section is comprised of a higher percentage of silica than the top samples, where it is present in a minor amount (Table 2). Hematite cement can also be observed as the second most abundant cement in the formation, while calcite and dolomite cements are found in rare amounts in a few samples. Hematite and chert

veins can be found unevenly distributed in the sandstone of the Hangu Formation. A minor amount of clay matrix can be identified in only three samples on the top of the Hangu Formation sandstone (Table 2). Based on (Folk, 1968), the content of quartz, feldspar, and lithics in the Hangu Formation sandstones was recalculated to 100% (Table 3). Correspondingly, the sandstones can be classified as sub-arkose, arenite, and arkose (Fig. 8).

[Fig. 8 about here.]

Fig. 8. Mineralogical classification of the sandstones of the Hangu Formation on a QFL diagram (Folk, 1968).

Table 2 Mineralogical composition of the Hangu Formation sandstone. Metam., Metamorphic; Sedim., Sedimentary; Limest., Limestone

[Table 2 about here.]

Table 3 Recalculated sandstone detritus of the Hangu Formation.

[Table 3 about here.]

4.3.1. Sub-arkose facies

This sandstone facies directly overlies the previously described bauxite deposits. The fresh color of this sandstone is light gray, whereas the weathered rocks attain rather dark brown colors. This facies is relatively coarse-grained, pebbly, and appears to be fractured. The total thickness of the sub-arkose within the studied Yagdaar Section is ca. 1.5 m, with individual beds reaching thicknesses of ca. 15 cm. The contained pebbles are generally 2–4 mm in size. A total of ten thin sections (YH1–YH10) represent this facies. Recalculated quartz percentages range between 87% and 94% (Table 3). The quartz grains are mostly polycrystalline (Qp) and are 0.05-1 mm in size (Fig. 9A-D). However, in a few samples, monocrystalline quartz (Qm) can also be observed (Fig. 9A–D). Most of the quartz grains are angular to subangular, with a few being subrounded. Reworked, rounded quartz grains are also found (Fig. 9D). The grains are poorly sorted but closely packed (Fig. 9C and E). Fractured quartz grains are filled with hematite, which shows parallel leaching due to previous contact with water (Fig. 9F).

In thin sections, recalculated feldspar percentages range from 6 to 11%. (Table 3; Fig. 9B). This facies lacks rock fragments and matrix (Table 2). Chert and hematite veins have a percentage of 4-6% and 1-4%, respectively (Table 2; Fig. 9C–E). Silica cement is the most common, with contents ranging from 3-22%, while hematite cement has contents ranging from 2-5%. In general, the facies can be described as a cherty silicate sub-arkose sandstone.

[Fig. 9 about here.]

Fig. 9. Photomicrographs of the sub-arkose thin sections of Sf_1: (A) close packing of polycrystalline quartz (X-PL); (B) plagioclase grain (X-PL); (C) orthoclase grains (X-PL); (D) detrital rounded quartz grain (X-PL); (E) hematite vein (X-PL); (F) parallel leaching of hematite (PPL).

4.3.2. Quartz-arenite facies

The quartz-arenite facies consist of coarse-grained, light gray sandstones with individual bed thicknesses ranging from 10 to 75 cm. In the Yadgaar Section, the total thickness of this facies ranges from 50 to 75 cm. This facies is represented by eight thin sections (YH11–YH18). The recalculated quartz percentages range from 95 to 98%. (Table 3). The majority of the quartz grains are monocrystalline, with a few polycrystalline quartz grains present in a few samples (Fig. 10A). The grains typically range in size from 0.05 to 1.5 mm. They are angular to subangular in shape, with non-undulatory quartz dominating and dissolution features (quartz replaced by silica cement) typically found in grain corners (Fig. 10B).

Recalculated percentages of feldspar range from 2–5% in this rock. Rock fragments and matrix are absent. In a few samples, hematite veins can be observed. Silica and hematite cements are found in almost equal amounts, with a range between 1–20% and 4–10%, respectively.

[Fig. 10 about here.]

Fig. 10. Textures and mineral content in the quartz-arenite sf_2: (A) close packing of the quartz grains; (B) dissolved quartz boundaries and silica cement; (C) alteration of biotite into muscovite and further change into chlorite; (D) alteration of orthoclase into sericite; (E) tourmaline grain; (F) pyrite grain and inclusion of igneous zircon in quartz.

Furthermore, a variety of alteration features can be observed, such as biotite being changed to muscovite while chlorite (Fig. 10C) and orthoclase are altered to sericite (Fig. 10D). In addition, tourmaline and igneous zircon inclusions in quartz have been observed (Fig. 10E and 10F).

4.3.3. Arkose facies

The topmost facies of the sandstone deposits of the Yadgaar Section is characterized by medium-grained arkose. The total thickness of this facies is 2 m, with individual beds ranging between ca. 10 and 24 cm in thickness. The color of the sandstone is dark brown to golden brown. Five thin sections represent this facies (YH19–YH23). Recalculated percentages of quartz display a range between 68–75%. Both monocrystalline and polycrystalline quartz grains are observed in almost equal amounts. The quartz grains are poorly sorted and fractured (Fig. 11A and B). The shape of the quartz grains varies from sub-angular to sub-rounded (Fig. 11A–D). In contrast to the previous facies, the corners of the quartz grains show less or no dissolution features.

Recalculated values of the feldspar grains range between 25–32% in this facies. Alteration zones in orthoclase and perthite grains (feldspar) indicate sericitization (Fig. 11B). Zircon grains can be observed in several samples (Fig. 11D and E). The typical concentration of hematite veins in rocks of this facies is between 1–4%. Hematite is also the most common cementing material, accounting for 3–5%. Silica cement may reach 1–2% of the total rock in the samples (Fig. 11F).

A minor clay matrix, ranging in content from 2–3%, can be found within a few thin sections encountered towards the top of this facies.

[Fig. 11 about here.]

Fig. 11. Texture and mineral content of the studied arkose samples sf_3: (A) large quartz grains; (B) K-feldspar (orthoclase) being altered to sericite; (C) perthite alteration into sericite and muscovite; (D) an opaque phase of zircon; (E) zircon inclusion in quartz; (F) hematite cement.

4.3.4. The mineralogical trend of the Hangu Formation sandstone

The petrographic studies on the sampled sandstones reveal a clear mineralogical trend from the base to the top of the studied section (Table 2). The modal mineralogical values of quartz, feldspar, and lithics are recalculated to infer their composition. The mean values are $Qt_{88}F_{28}L_{0.2}$ (Table 3). The range of lithic fragments (QmFLt %Lt) is 6–75%. Monocrystalline quartz (QmFLt%Qm) ranges from 0–79%. The majority of the samples from the base to the center only contain polycrystalline quartz. In the samples from the middle of the sandstone succession, suddenly, monocrystalline quartz starts to appear while polycrystalline quartz starts to decrease. Moving up the section, the monocrystalline quartz grains show a minor increase toward the top (Table 2). Feldspar (QmFLt%F) ranges from 2–25% (Table 3). Plagioclase can be observed in rare amounts in a few samples at the base of the section, while it occurs abundantly at the top. K-feldspar (orthoclase) is observed consistently throughout the formation. However, its abundance is highest in the top (arkose) and lowest in the middle facies (quartz arenite). Recalculated values of feldspar reveal that the average values of K-feldspar are much higher than plagioclase (Qm25 ± 1 P0.5 ± 0.2 K7.9 ± 1; Tables 2 and 3).

4.4. Integrated facies assessment of the Hangu Formation limestone

[Table 4 about here.]

The relatively thin limestone layers (12 cm) at the top of the Hangu Formation can be classified as mudstone according to the Dunham classification (Table 4). Micrite is the dominant constituent of the rock, with hematite and calcite veins as minor constituents. Bioclasts are partially to completely micritized and are frequently replaced by hematite. Pyrite is found in both framboidal and hematized forms. Quartz grains can also be found randomly scattered in small amounts.

Table 4. Mineralogical composition of the thin sections from limestone facies.

5. Discussion

5.1. Interpretations from petrographic indicators of bauxite

Bauxite is a residual sedimentary rock rich in alumina and iron oxide and depleted in silica and alkalis (Sidibe and Yalcin, 2019). The most common climatic conditions for the formation of bauxite are tropical to subtropical conditions with abundant rainfall. The rate and intensity of weathering can be influenced by the type of bedrock, chemical conditions, groundwater pH, tectonic setting, and geomorphology (Nurhawaisyah et al., 2021). The key parameters for the rate of chemical weathering that converts laterite to bauxite are water abundance, time, and temperature (Ramadhan et al., 2014).

Diaspore and gibbsite are the most common hydrated aluminum oxide forms (Sidibe and Yalcin, 2019) found in bauxite deposits. Diaspore is the dominant mineral in the majority of the collected samples, particularly at the base and the center of the deposit, but it was found to be absent in the samples from the top of the deposit (Figs. 6 and 7). Diaspore is typical of karst bauxite (Ling et al., 2015; Yang et al., 2017b). The carbonates of the underlying Abbottabad Formation are characterized by a karst depression on the carbonate platform (Fig. 3). The discovery of diaspore-dominated strata above the karst setting therefore confirms that the lower to middle portion of the facies is a karst bauxite (Table 1).

Gibbsite is the most common aluminum-rich mineral in samples from the center to the top of this facies (Fig. 7; Table 1). The presence of gibbsite stipulates that these samples belong to the lateritic bauxite (Nurhawaisyah et al., 2021). The high percentage of gibbsite may suggest a high economic value of this lateritic bauxite, as it is the most important source of aluminum in bauxite in the world (Table 1). The occurrence of both types, gibbsite and diaspore, in one stratum is an interesting discovery that has been rarely reported in the world (Fig. 1; c.f. (Schulte and Foley, 2014)). This inverse relation between diaspore and gibbsite therefore confirms that the lower part of bauxite is karst bauxite and the middle to top portion of the bauxite deposit is a lateritic bauxite (Table 1; Fig 12A). This interpretation is further supported by observations from the field study that show that the lower contact of the Hangu Formation's bauxite is markedly unconformable with the underlying Cambrian dolostone of the Abbottabad Formation (Fig. 2B). Previous studies (Ramanaidou, 2009) have shown that the formation of gibbsite may also be related to the existing morphology and the formation of a paleoslope. This may be seen as evidence for the deposition of the lateritic bauxite on top of the sloping karst landscape. Commonly, the precursor mineral for gibbsite is kaolinite Al2O3Si2O5(OH)4 after the removal of Si from granites. The kaolinite, in

turn, can then alter further to gibbsite Al (OH)3 (Figs. 6E and 12B) (Violante et al., 2005; Elias and Alderton, 2020). Furthermore, when the gibbsite is dehydrated, it can alter into a monohydrate diaspore (Goldman, 1955).

The diaspore shows an inverse relationship with gibbsite and kaolinite (Table 1; Fig. 12A). Its existence in the studied section may be an indication that most of the gibbsite has been frequently altered into the diaspore. However, the gibbsite is directly related to the occurrence of kaolinite (kaolinite is the pseudomorph of goethite; Fig. 12B) within the section. The presence of kaolinite in the samples suggests that the precursor rock had a high concentration of gibbsite (Table 1). A high presence of kaolinite generally indicates a plateau environment. Goethite indicates a slope, while hematite indicates a slope–plateau environment (Ramanaidou, 2009). For instance, weathered dolerite near a sloping plateau may be the source of hematite. In a slope environment, hematite grains are depleted in the cementing material and thus fail to preserve the original structure of hematite. Mineral migration occurs on this slope, where hydrous aluminum oxides and clay minerals are transported to their final place of deposition (Allen, 1952). The evidence for mineral alteration indicates an elevated provenance that was exposed to high rainfall and intense chemical and physical weathering along a slope. The rock-water interaction in such an unstable area resulted in mineral alterations and an environmental shift from high-slope weathering towards a low-lying area (Hara and Tsuchiya, 2004). A minor amount of biotite in the samples at the top of the bauxite (Table 1) indicates that the precursor rock may have been granodiorite, basalt, or gabbro (Nurhawaisyah et al., 2021).

A set of mineral variation diagrams is used to find the correlation between different constituents of bauxite in the Yadgaar Section. It can be observed that the correlation between gibbsite and diaspore is strongly negative (Fig. 12A), whereas it is moderately positive between

gibbsite and kaolinite (Fig. 12A). Furthermore, the correlation between hematite and kaolinite is strongly negative (Fig. 12C), while it is moderately positive between hematite and diaspore (Fig. 12D). The correlations between hematite and gibbsite, as well as diaspore and kaolinite, are both

[Fig. 12 about here.]

Fig. 12. Mineral variation diagrams for the studied bauxite minerals. (A) diaspore vs. gibbsite; (B) kaolinite vs. gibbsite; (C) kaolinite vs. hematite; (D) diaspore vs. hematite; (E) gibbsite vs. hematite; (F) kaolinite vs. diaspore.

moderately negative (Fig. 12E and F). Most of the diagrams show negative correlations. This indicates a very strong process of mineral alteration. High amounts of mineral alteration point towards an unstable chemical and physical environment under tropical or humid conditions (Ueki and Iwamori, 2017; Pazand et al., 2021).

5.2. Paleoclimate, sedimentary environment, and facies associations

The IB in Pakistan consists of Precambrian–Cenozoic strata (Table 5). Most of the Paleozoic–Mesozoic strata start to disappear as progress from the Southern Indus Basin (SIB) to the UIB (Table 5; (Bilal et al., 2022b). This is marked by an unconformity, which is overlain by the studied bauxite deposits (Table 5; Fig 13A). After intense chemical weathering and leaching in a tropical to subtropical environment, the remnants of the weathered and eroded Permian–Cretaceous strata gave rise to the karst bauxite of the Hangu Formation (Khan et al., 2022a). This process was prolonged for a significant time, resulting in the enrichment of aluminum hydroxide and minor impurities of iron oxide and silica.

After the geological events of uplift and erosion in the southern part of the Central Indus Basin (CIB), the deposition of karst bauxite took place (Singh and Khan, 2017). The karst bauxite deposits formed in mildly brackish mires on the backside of barrier systems (flood tidal delta planes) on karstified limestone (Yang et al., 2017a). A unique landform of irregular surfaces has been identified as karst depression, which was developed (before the deposition of bauxite) due to the dissolution of underlying carbonate beds. In the Yadgaar Section, a typical cockpit-type karst depression could be identified (Fig. 13A).

Just above this karst bauxite (B_1), the lateritic bauxite (B_2) was deposited in the region when the rate of chemical weathering started to become more intense (Fig. 13B). Intensive degradation of excessive organic matter in reducing conditions is often associated with coal (Kalaitzidis et al., 2010; Yang et al., 2022). The thin coal layer (C_1) may have formed due to similar conditions (Fig. 13C). The generation of coal was followed by an increased input of siliciclastic material ($Sf_{1–3;}$ Fig. 13D–F), which was subsequently followed by the formation of further coal ($C_{2;}$ Fig. 13G) and, finally, the formation of limestone (L; Fig. 13H) in the basin.

Table 5. Stratigraphic sequences in the different areas of the Indus Basin (IB) (modified after (Bilal et al., 2023).

[Table 5 about here.]

The thin coal layer (C_1) represents the initial development of a failed peatland (Fig. 13C), which was overloaded by the clastic influx (Fig. 13D–F) just after its formation. Peatland surfaces are often prone to dramatic failures due to various in-situ factors such as rainfall and drought

conditions (Dise, 2009; Dai et al., 2020; O'connor and Courtney, 2020). Sulfate-rich acidic solutions observed in the outcrop are the product of the oxidation of pyrite in the coal layer (Fig. 4D). This oxidation of coal reportedly occurs at the advanced stage of peat formation in a lagoon or drainage-rich continental transgressive environment (Kalaitzidis et al., 2010). These facies are equivalent to the FZ9B (humid near-coast brackish regions) facies of (Flügel and Munnecke, 2010).

[Fig. 13 about here.]

Fig. 13. (A) Histogram of the Hangu Formation profile; (B–H) evolution of the topology in response to tectonic events, sedimentary environment and facies shift during the deposition of the facies suit.

The clastic influx led to the deposition of three fluvial-deltaic intercalated sandstone facies (Figs. 13D–F). The pebbly sub-arkose (Sf_1) at the base of the sandstone succession indicates deposition under high-energy conditions in a transitional fluvial to deltaic or nearshore environment (Fig. 13D) (Van De Kamp, 2010; Jafarzadeh N et al., 2022). This is also supported by the scarcity of fossils (Aigbadon et al., 2022). Furthermore, the absence of cross-bedding indicates a strong unidirectional paleocurrent, which also points toward a facies association with high-energy fluvial conditions in a delta system (Okolo et al., 2020; Okoro et al., 2020). The diagram in Fig. 14 further confirms that the parental environment was sub-humid (also see Table 6). The high amount of silica cement (Fig. 9C) indicates that the basin may have exhibited acidic conditions, which led to the dissolution of silica. However, during the deposition of this rock, the conditions turned towards alkalinity (Montgomery et al., 2000; Haihua et al., 2015; Li et al., 2020). Dissolved quartz boundaries further confirm the presence of initial acidic conditions (Fig. 9C). In

the later alkaline conditions, silica cement was deposited in pores and in the free space between the grains (Perri et al., 2008; Barbera et al., 2011). The low mica contents (Table 2) in the sub-arkose provide evidence for sub-humid conditions. Sub-humid conditions facilitate the alteration of the mica during the transportation process (Scarciglia et al., 2005; Scarciglia et al., 2007). Parallel hematite lines indicate the leaching of hematite on a wet, sloping medium (Fig. 9F).

[Fig. 14 about here.]

Fig. 14. Paleoclimatic interpretation from the QFL ternary diagram for the sandstones of the Hangu Formation (based on (Suttner and Dutta, 1986).

A humid climate aided in the transgression on the carbonate platform and the quick sedimentation rate in the fluvial continental environment. These humid conditions caused the deposition of arenite (Sf_2) on top of the sub-arkose and facilitated the dissolution of less stable minerals (Fig. 13E). In a warm to hot climate with severe chemical weathering, this facies reflects a coastal or shore depositional environment (Fig. 13E) (Van De Kamp, 2010). The rock's super-mature quartz (Fig. 10A) may have undergone extensive eolian reworking before being carried to coastal areas like the foreshore/backshore, tide flat, shoreface, delta, or mouth/lower delta plain (Chakraborty and Sensarma, 2008; Barbera et al., 2011; Lorentzen et al., 2018; Seraine et al., 2020). The parental setting is depicted in Fig. 14 as humid to hot-humid.

Textural interpretations show that the close packing of the quartz grains indicates that the rock is arenite, while the angular to sub-angular appearance depicts a less distant and high-energy transport (Fig. 10A). The absence of a matrix and the high abundance of quartz (Table 2) illustrate intense weathering and a transport process that removed the matrix from the detritus. The absence of rock fragments suggests that the detritus does not originate from an orogeny. Furthermore, this

facies possesses a high content of silica cement and small amounts of chert. Increasingly acidic conditions in the basin dissolved high levels of silica, which were eventually deposited under alkaline conditions during the formation of the arenite facies. Dissolved quartz boundaries further confirm the initial presence of intense acidic conditions in the basin (Fig. 10B). The high amount of silica cement in the arenite sandstone facies also confirms a high-energy depositional setting in a subaerial (delta) sedimentary environment (Table 6; Fig. 13E). It goes on to say that there was enough time for the sand grains to cement together and the silica to precipitate in a warm and arid environment. The alteration of orthoclase and biotite into muscovite and sericite (Figs. 10C and 10D) indicates a chemically unstable environment. Mica depletion in this facies (Table 2) points to hot and humid conditions, which altered the mica during transport.

Arkose is a versatile rock that can be deposited in various sedimentary environments. Very often, it is associated with high-energy alluvial, fluvial, and coastal environments (Jafarzadeh and Hosseini-Barzi, 2008; Sunderlin et al., 2014; Seraine et al., 2020). The arkose facies (Sf_3) of the Hangu Formation represents high-energy, braided river channels in a fluvial environment with deposition in a semi-arid climate (Table 6; Fig. 13F). High amounts of feldspar (Table 2) suggest arid to semi-arid and subtropical–tropical climates, with a possible origin from granitic rocks (Van De Kamp, 2010). The diagram in Fig. 14 suggests an arid to semi-arid environment for the formation of this facies. The dominant hematite cement (Fig. 11F) in this facies points towards a subaerial sedimentary environment associated with a river and/or coastal plain. Oxidation of iron-rich minerals in a subaerial environment led to the formation of hematite. During the deposition of this facies, the sediments were exposed to the atmosphere for a particular time, which facilitated the oxidation. Zoning alteration in orthoclase (Fig. 11B) and muscovite into sericite (Fig. 11C) indicates a chemically unstable environment. However, the quartz boundaries are not dissolved

(Fig. 11A–F) as compared to previously described facies, which indicates a shift in chemical conditions within the basin from acidic to alkaline (Haihua et al., 2015; Oye et al., 2020).

An additional coal layer (Fig. 13J) is found above the sandstones, which may have formed after a regression in the area due to peatland formation in a low-lying area. As a result, the coal-sandstone-coal sequence could be evidence for a rhythmic repetition of transgression and regression cycles during the continental-marine transition. The formation of the peatland was a relatively complex process. Several factors are known that may have influenced this, including a de-oxygenated environment, slow-moving water, heavy rainfall, a faster rate of plant productivity, a high water table, and the area's poor drainage capacity (Kreuzburg et al., 2018). Furthermore, low subsurface flow and slow decomposition resulted in the enrichment of decaying organic matter (Dise, 2009). Continuous weight addition caused load compression and increased heat in the peat's organic matter, resulting in coal formation (Fig. 13G). The water influx in the peatland environment was most likely caused by river floods or seawater following a regression. The area of deposition was most likely characterized by a low-lying topography, such as a coastal plain or river delta (Fig. 13G) (Kreuzburg et al., 2018), with relatively high subsidence.

Soon after the deposition of the coal, a transgression event led to the deposition of a thin layer of marly limestone (mostly concealed and rarely exposed), a fine-grained micritic carbonate rock that can be classified as mudstone according to Dunham (1962). This transitional phase marked the shift from a continental to a shallow marine environment (Figs. 2K and 5E). The presence of abundant hematite in this facies' samples (Table 4) indicates an oxic environment in a shallow marine setting, whereas the low amount of pyrite reflects de-oxic conditions. This suggests that the hematite formed *in situ* in an oxic environment and began to change into pyrite when the conditions changed to deep water and de-oxygenated conditions prevailed (Bilal et al., 2022b).

Minor quartz grains within the carbonate rock may also be evidence for pedogenic carbonate, which is most likely deposited in a continental–marine transitional environment associated with karst settings (Table 6). Pedogenic carbonates indicate the reworking of both carbonate and clastic components (Flügel and Munnecke, 2010). Therefore, this facies may be equivalent to the FZ9B (near-coastal brackish regions) and FZ10 (paleokarst, caliche, and other terrestrial and terrestrial-to-marine settings) facies (Flügel and Munnecke, 2010). The facies' sedimentary environment is transitional terrestrial–marine, and it most likely formed at the platform interior's edge in a brackish and humid environment (Table 6; Fig. 13K).

Table 6 Facies descriptions and their interpretations.

[Table 6 about here.]

5.3. Facies shift under sedimentary dynamics

Within a specific area, a facies shift is defined as a gradual change in the characteristics of sedimentary rock formations, such as rock types, mineral content, texture, thickness, and sedimentary structures. Changes in the dynamics of a sedimentary environment cause these shifts, which are further influenced by factors such as sea level changes, tectonics, and climate change (Allen and Johnson, 2011).

The facies shift within the Hangu Formation and its associated sedimentary dynamics are pioneering work. Based on field studies and petrographic results from the Hangu Formation, a facies shift has been revealed to have formed within a complex environment (Fig. 13A–H). Overall, the studied continental to marine transitional facies demarcates two bauxites, two coal,

three sandstone, and one limestone deposit in the Yadgaar Section (Table 6). After an uplift of the Permian basin on the Indian Plate, the area was exposed to a warm and humid climate (Fig. 14) (Singh and Khan, 2017). This triggered an extreme erosion rate of the strata, which in turn resulted in the deposition of bauxite in the lowland region (Fig. 13B). Within the study area, the dissolution of the underlying carbonate rock developed a karst depression, which eventually led to the deposition of karst bauxite at the base of the section. The climate during that time was characterized by low rainfall and less intense weathering. When the climate started to become harsher, it led to a shift in facies. Hence, a facies shift took place from the karst bauxite towards the lateritic bauxite (Fig. 13B). The climate shifted to a high-rainfall tropical region, which eventually led to the formation of peatland (Van De Kamp, 2010). A transgressive event converted this lowland into peatland for a short period (with the deposition of coal; Fig. 13C). However, this did not last long because a sudden sedimentary shift toward fluvial conditions took place, which provided a heavy clastic influx in the area (Fig. 13D). This could have occurred as a result of a new topological change that caused a shift from low-angle topology to the development of a medium-steep slope. This tectonically induced increasing slope topology possibly caused the formation of high-energy river channels and deltas, allowing for an increased sedimentation rate in the area (Fig. 13D). This resulted in a further facies shift from bauxite towards the sedimentation of coarse-grained, feldspar-rich clastic detritus and the formation of sub-arkose sandstone.

Increasing humidity (Fig. 14) raised the extent of chemical weathering and caused feldspar grains in the sediment to dissolve (Table 2), resulting in a transition from sub-arkose to quartz-arenite sandstone (Table 3). While the fluvial environment persisted, along with an ongoing transgression, the climate shifted to semi-arid conditions, resulting in the deposition of the arkose facies (Fig. 13E).

With increasing subsidence in the area, the conditions for the formation of mature peatlands began to emerge. The low-lying areas became flooded, while faster sedimentation rates prevailed and plant debris started to accumulate within a de-oxygenated environment (Kreuzburg et al., 2018). Heavy rainfall aided not only the accumulation of plant debris but also the inflow of river floods and associated detritus. As a result, the facies shifted from sandstone to coal (Fig. 13F–G). These conditions persisted for a short time before the transgression continued, resulting in a rise in the water level to the point where the area became a shallow shelf platform (Bilal et al., 2022b) (Fig. 13H) that became part of the Ceno-Tethys Ocean (Fig. 5E). As a result, the facies shifted from coal to a shallow shelf marly-limestone (FZ9B–10) (Fig. 5E).

This limestone facies was the last or topmost lithology of the Hangu Formation. The facies has direct contact with the base of the overlying Lockhart Limestone, which is reported as a mudstone–wackestone facies deposited at the toe of a slope and is equivalent to FZ4 facies (Flügel and Munnecke, 2010). This shows an abrupt jump in the facies from FZ9B and FZ10 to the FZ4 facies (Flügel and Munnecke, 2010). In a carbonate platform model, both of these facies can be found at almost opposite ends of the continuum. On the carbonate platform, FZ9B and FZ10 are present on the shallower side of the edge, while FZ4 is present at the deeper water levels where de-oxic and a-photic zones prevail (Flügel and Munnecke, 2010). This facies shift indicates a quick transgression in the area, which points towards an unusual event that may have caused the transgression and sea level rise.

5.4. Tectonic framework and basin evolution

The Indian Shield basement rocks within the IB are part of Gondwana, on which Precambrian to recent sedimentary strata have accumulated (Shah, 2009). However, the absence of Paleozoic–Mesozoic strata in the study area represents a massive unconformity (Bilal et al., 2022a) (Table

5). As a result, the Paleocene Hangu Formation directly overlies the Precambrian–Cambrian sediments within the basin (Fig. 4A). The reasons for the development of the unconformity are several. One of the reasons was a large-scale regional uplift event during the Permian that affected the Aravalli Range, Kirthar Orogen, Nagar Parker, and Melani Ranges and led to wide-ranging erosion on the Indian Plate (Singh and Khan, 2017; Khan et al., 2022b). This uplift not only played an important role in the shaping of the IB (formation of the Salt Range), Himalayas, and Tibetan Plateau but also affected the climatic conditions of the region by promoting increased aridity and the formation of a desert environment (DiPietro et al., 2021). Furthermore, the Indo-Eurasian intra-oceanic subduction in the Tethys Ocean (Fig. 15A–B) during Triassic–Jurassic times massively shaped the physio-geological conditions of the basin and eventually led to the appearance of the Kohistan Island Arc (KIA) in the Tethys Ocean (Fig. 15B) (Bignold and Treloar, 2003; Khan et al., 2009).

The excessive erosion led to the deposition of bauxite on the evolving carbonate ramp platform in the Tethys Ocean (Fig. 13B). The ongoing interoceanic subduction terminated its activity during the closure of the Tethys Ocean. During this phase, the Indian Plate collided with the KIA, which allowed the transgressive epeiric sea incursion inward from the plate margins (Fig. 16A–B) (Bilal et al., 2022c). Active tectonism prevailed over those conditions, which facilitated the deposition of the described facies of the Hangu Formation (Fig. 16B). These conditions included episodic subsidence throughout the deposition of the Hangu Formation. The formation of peatland was followed by a clastic sedimentary influx with alluvial–deltaic conditions developing on the plate margins (Fig. 13C–F). It is thought that the development of a sedimentary environment and subsidence episodes in the study area strongly persisted due to ongoing convergent tectonism in the north (KIA) and a divergent push from the south (Figs. 15 and 16).

[Fig. 15 about here.]

Fig. 15. (A) Regional tectonism from the Late Cretaceous to the Middle Paleocene around the Tethys Ocean (modified after (Chatterjee and Bajpai, 2016). The red square shows Fig. 15B. (B) Tectonic model showing intra-oceanic subduction of the Indo-Eurasian plates, related processes, and the sedimentary environment at the initial time of the deposition of the Hangu Formation (modified after (Yang et al., 2019).

[Fig. 16 about here.]

Fig. 16. (A) Regional tectonism from early to middle Paleocene around the Tethys Ocean (modified after (Chatterjee and Bajpai, 2016). The red square shows Fig. 15B. (B) Tectonic model showing the collision phase of the Indian continental plate and the KIA and its relationship with the climatic conditions and the sedimentary environment during the time of the deposition of Hangu Formations' facies suit (modified after (Yang et al., 2019).

The formation of low land under the effect of load subsidence in the foredeep was a geotectonic process associated with the formation of an intra-oceanic arc (KIA) (Khan et al., 2009). The epeiric sea formation was the key factor that converted this subsided part into peatland, which in turn facilitated the deposition of coal. Active tectonism and rock strain near the hinterland during the Himalayan orogenic cycle converted this facies into tectonically deformed coal (TDC) (Wang et al., 2020; Khan et al., 2022a). The continuation of the Indo-Eurasian intra-oceanic subduction and the rise of the KIA led to an extension of the epeiric sea conditions towards the continent, where shallow shelf conditions started to develop (Figs. 13H and 15B) that eventually facilitated the

deposition of the marly limestone at the top of the Hangu Formation. The substantial differences in the sedimentary environments of the limestone at the top of the Hangu Formation and the first facies at the base of the overlying Lockhart Limestone (Bilal et al., 2022b) point to a significant tectonic event at that period. This was the time (60 Ma) when India collided with the KIA in the north, which caused high rates of subsidence and a rapid transgression of sea water in the study area (Fig. 15B) (Chatterjee and Bajpai, 2016). As a consequence, the facies changed from shallow marine (brackish) to deep marine conditions, which is convincing evidence that regional tectonics influenced how the corresponding facies were deposited.

6. Conclusion

The Paleocene Hangu Formation of the Yadgaar Section is made up of several sedimentary facies, such as residual, clastic, biochemical, and chemical rocks. This work demonstrated that the investigated bauxite, sandstone, limestone, and coal facies were deposited in karst landscapes, fluvial near-shore to deltaic, shallow marine platform environments, and peatland catchments, respectively. The described facies and their corresponding sedimentary environments strongly suggest that their deposition took place during a continental-to-marine transition. The paleoclimatic conditions during the deposition of these facies association were intense humid, sub-humid to semi-arid, humid tropical to near coast brackish humid, respectively. The extensive sedimentological observations reveal a strong link between tectonism, sedimentation, and climatic control. In particular, the regional tectonism controlled and promoted the continuous shifts in the sedimentary environment, while the availability of water throughout the episodic transgression and regression within the studied area influenced climatic conditions and rock weathering. All the aforementioned points lead to the conclusion that on the active continental margin, the regional

active tectonism created a physio-geological environmental mechanism that caused the development of particular continental–marine transitional facies.

Declaration of competing interest

The authors declare that they have no known competing financial interests or personal relationships that could have appeared to influence the work reported in this paper.

Data availability

The data used to support the findings of the study are included in the article. Data will be made available on request.

Acknowledgments

This study was financially supported by the China-ASEAN Maritime Cooperation Fund Project (grant No.12120100500017001) and the National Natural Science Foundation of China (grant No. 41972146).

References

Abbassi, S., Edwards, D.S., George, S.C., Volk, H., Mahlstedt, N., di Primio, R., Horsfield, B., 2016. Petroleum potential and kinetic models for hydrocarbon generation from the Upper Cretaceous to Paleogene Latrobe Group coals and shales in the Gippsland Basin, Australia. Organic Geochemistry 91, 54-67.

Afzal, J., Williams, M., Aldridge, R.J., 2009. Revised stratigraphy of the lower Cenozoic succession of the Greater Indus Basin in Pakistan. Journal of Micropalaeontology 28, 7-23.

Aigbadon, G.O., Christopher, S.D., Akudo, E.O., Akakuru, O.C., 2022. Sedimentary facies and textural characteristics of Cretaceous sandstones in the southern Bida Basin, Nigeria: Implication for reservoir potential and depositional environment. Energy Geoscience 3, 323-341.

Al-Rajhi, A., Abbasi, I.A., Razin, P., Al Harthy, A., 2021. Sedimentology of mixed siliciclastic-carbonate system in a structurally constrained Paleogene basin: Eocene Musawa Formation in Eastern Oman Mountains. Journal of African Earth Sciences 173, 104020.

Allen, J.L., Johnson, C.L., 2011. Architecture and formation of transgressive–regressive cycles in marginal marine strata of the John Henry Member, Straight Cliffs Formation, Upper Cretaceous of Southern Utah, USA. Sedimentology 58, 1486-1513.

Allen, V.T., 1952. Petrographic relations in some typical bauxite and diaspore deposits. Geological Society of America Bulletin 63, 649-688.

Amorosi, A., Colalongo, M.L., Fusco, F., Pasini, G., Fiorini, F., 1999. Glacio-eustatic control of continental–shallow marine cyclicity from late Quaternary deposits of the southeastern Po Plain, northern Italy. Quaternary research 52, 1-13.

Awan, R.S., Liu, C., Aadil, N., Yasin, Q., Salaam, A., Hussain, A., Yang, S., Jadoon, A.K., Wu, Y., Gul, M.A., 2021. Organic geochemical evaluation of Cretaceous Talhar Shale for shale oil and gas potential from Lower Indus Basin, Pakistan. Journal of Petroleum Science and Engineering 200, 108404.

Badshah, M., Gnos, E., Jan, M., Afridi, M., 2000. Stratigraphic and tectonic evolution of the northwestern Indian plate and Kabul Block. Geological Society, London, Special Publications 170, 467-476.

Baig, M.S., Munir, M.-u.-H., 2007. Foraminiferal biostratigraphy of Yadgar area, Muzaffarabad Azad Kashmir, Pakistan. Journal of Himalayan Earth Sciences 40.

Barbera, G., Critelli, S., Mazzoleni, P., 2011. Petrology and geochemistry of cretaceous sedimentary rocks of the Monte Soro unit (Sicily, Italy): constraints on weathering, diagenesis, and provenance. The Journal of Geology 119, 51-68.

Basharat, M., Khan, A.F., Riaz, M.T., Sadaf, R., 2020. Application of rock mass classification to evaluate rock properties, NW Himalayas, Pakistan. Acta Geodyn. Geomater 17, 453-468.

Basilone, L., Perri, F., Sulli, A., Critelli, S., 2017. Paleoclimate and extensional tectonics of short-lived lacustrine environments. Lower Cretaceous of the Panormide Southern Tethyan carbonate platform (NW Sicily). Marine and Petroleum Geology 88, 428-439.

Bignold, S., Treloar, P., 2003. Northward subduction of the Indian Plate beneath the Kohistan island arc, Pakistan Himalaya: new evidence from isotopic data. Journal of the Geological Society 160, 377-384.

Bilal, A., Mughal, M.S., Janjuhah, H.T., Ali, J., Niaz, A., Kontakiotis, G., Antonarakou, A., Usman, M., Hussain, S.A., Yang, R., 2022a. Petrography and Provenance of the Sub-Himalayan Kuldana Formation: Implications for Tectonic Setting and Palaeoclimatic Conditions. Minerals 12, 794.

Bilal, A., Yang, R., Fan, A., Mughal, M.S., Li, Y., Basharat, M., Farooq, M., 2022b. Petrofacies and diagenesis of Thanetian Lockhart Limestone in the Upper Indus Basin (Pakistan): Implications for the Ceno-Tethys Ocean. Carbonates and Evaporites 37, 1-19.

Bilal, A., Yang, R., Janjuhah, H.T., Mughal, M.S., Li, Y., Kontakiotis, G., Lenhardt, N., 2023. Microfacies analysis of the Palaeocene Lockhart limestone on the eastern margin of the Upper Indus Basin (Pakistan): Implications for the depositional environment and reservoir characteristics. The Depositional Record 9, 152-173.

Bilal, A., Yang, R., Mughal, M.S., Janjuhah, H.T., Zaheer, M., Kontakiotis, G., 2022c. Sedimentology and Diagenesis of the Early–Middle Eocene Carbonate Deposits of the Ceno-Tethys Ocean. Journal of Marine Science and Engineering 10, 1794.

Bogatyrev, B., Zhukov, V., Tsekhovsky, Y.G., 2009. Formation conditions and regularities of the distribution of large and superlarge bauxite deposits. Lithology and Mineral Resources 44, 135-151.

Boni, M., Rollinson, G., Mondillo, N., Balassone, G., Santoro, L., 2013. Quantitative mineralogical characterization of karst bauxite deposits in the southern Apennines, Italy. Economic Geology 108, 813-833.

Calkins, J.A., Matin, A.A., 1973. The geology and mineral resources of the Garhi Habibullah quadrangle and the Kakul area, Hazara District, Pakistan. US Geological Survey], US.

Chakrabarti, B.K., 2016. Geology of the Himalayan belt: deformation, metamorphism, stratigraphy. Elsevier.

Chakraborty, T., Sensarma, S., 2008. Shallow marine and coastal eolian quartz arenites in the Neoarchean-Palaeoproterozoic Karutola Formation, Dongargarh Volcano-sedimentary succession, central India. Precambrian Research 162, 284-301.

Chatterjee, S., Bajpai, S., 2016. India's northward drift from Gondwana to Asia during the Late Cretaceous-Eocene. Proceedings of the Indian National Science Academy 82, 479-487.

Chaudhuri, A., Banerjee, S., Le Pera, E., 2018. Petrography of Middle Jurassic to Early Cretaceous sandstones in the Kutch Basin, western India: Implications on provenance and basin evolution. Journal of Palaeogeography 7, 1-14.

Chaudhuri, A., Schönig, J., Le Pera, E., von Eynatten, H., Chauhan, G., Lünsdorf, N.K., 2023. Provenance changes revealed by a multi-proxy approach to sandstone analysis and its implications on palaeogeography: Mesozoic Kutch Basin, India. Sedimentary Geology 452, 106411.

Combes, P.-J., 1990. Typologie, cadre géodynamique et genèse des bauxites françaises. Geodinamica Acta 4, 91-109.

Craig, J., Hakhoo, N., Bhat, G., Hafiz, M., Khan, M., Misra, R., Pandita, S., Raina, B., Thurow, J., Thusu, B., 2018. Petroleum systems and hydrocarbon potential of the North-West Himalaya of India and Pakistan. Earth-science reviews 187, 109-185.

Critelli, S., De Rosa, R., Platt, J.P., 1990. Sandstone detrital modes in the Makran accretionary wedge, southwest Pakistan: Implications for tectonic setting and long-distance turbidite transportation. Sedimentary Geology 68, 241-260.

Critelli, S., Garzanti, E., 1994. Provenance of the lower Tertiary Murree redbeds (Hazara-Kashmir Syntaxis, Pakistan) and initial rising of the Himalayas. Sedimentary Geology 89, 265-284.

Critelli, S., Ingersoll, R.V., 1994. Sandstone petrology and provenance of the Siwalik Group (northwestern Pakistan and western-southeastern Nepal). Journal of Sedimentary Research 64, 815-823.

Critelli, S., Martín-Martín, M., 2022. Provenance, paleogeographic and paleotectonic interpretations of Oligocene-Lower Miocene sandstones of the western-central Mediterranean region: A review. Journal of Asian Earth Sciences: X, 100124.

Dai, S., Bechtel, A., Eble, C.F., Flores, R.M., French, D., Graham, I.T., Hood, M.M., Hower, J.C., Korasidis, V.A., Moore, T.A., 2020. Recognition of peat depositional environments in coal: A review. International Journal of Coal Geology 219, 103383.

Dar, Q.U.Z., Renhai, P., Ghazi, S., Sajid, Z., Wahab, A., Zubair, R.A., Aziz, T., 2021. The Precambrian Hazara Formation from Hazara Mountains, Northern Pakistan. Arabian Journal of Geosciences 14, 1-17.

DeCelles, P., Kapp, P., Gehrels, G., Ding, L., 2014. Paleocene-Eocene foreland basin evolution in the Himalaya of southern Tibet and Nepal: Implications for the age of initial India-Asia collision. Tectonics 33, 824-849.

DiPietro, J.A., Pullen, A., Krol, M.A., 2021. Geologic history and thermal evolution in the hinterland region, western Himalaya, Pakistan. Earth-Science Reviews 223, 103817.

Dise, N.B., 2009. Peatland response to global change. Science Advances 326, 810-811.

Ehsan, M., Gu, H., Ali, A., Akhtar, M.M., Abbasi, S.S., Miraj, M.A.F., Shah, M., 2021. An integrated approach to evaluate the unconventional hydrocarbon generation potential of the Lower Goru Formation (Cretaceous) in Southern Lower Indus basin, Pakistan. Journal of Earth System Science 130, 1-16.

Elias, S., Alderton, D., 2020. Encyclopedia of Geology. Academic Press.

Escobar, M., Márquez, G., Suárez-Ruiz, I., Juliao, T., Carruyo, G., Martínez, M., 2016. Source-rock potential of the lowest coal seams of the Marcelina Formation at the Paso Diablo mine in the Venezuelan Guasare Basin: Evidence for the correlation of Amana oils with these Paleocene coals. International Journal of Coal Geology 163, 149-165.

Flügel, E., Munnecke, A., 2010. Microfacies of carbonate rocks: analysis, interpretation and application. Springer.

Folk, R.L., 1968. Petrology of sedimentary rocks: Hemphill's. Austin, Texas 170, 85.

Friederich, M.C., Moore, T.A., Flores, R.M., 2016. A regional review and new insights into SE Asian Cenozoic coal-bearing sediments: Why does Indonesia have such extensive coal deposits? International Journal of Coal Geology 166, 2-35.

Gaetani, M., Zanchi, A., Angiolini, L., Olivini, G., Sciunnach, D., Brunton, H., Nicora, A., Mawson, R., 2004. The Carboniferous of the Western Karakoram (Pakistan). Journal of Asian Earth Sciences 23, 275-305.

Gu, J., Huang, Z., Fan, H., Jin, Z., Yan, Z., Zhang, J., 2013. Mineralogy, geochemistry, and genesis of lateritic bauxite deposits in the Wuchuan–Zheng'an–Daozhen area, Northern Guizhou Province, China. Journal of Geochemical exploration 130, 44-59.

Guyonnet-Benaize, C., Lamarche, J., Masse, J.-P., Villeneuve, M., Viseur, S., 2010. 3D structural modelling of small-deformations in poly-phase faults pattern. Application to the Mid-Cretaceous Durance uplift, Provence (SE France). Journal of Geodynamics 50, 81-93.

Haihua, Z., Zhong, D., Jingli, Y., Haitao, S., Xiaobing, N., LIANG, X., Yuan, Y., Xin, L., 2015. Alkaline diagenesis and its effects on reservoir porosity: A case study of Upper Triassic Chang 7 Member tight sandstone in Ordos Basin, NW China. Petroleum Exploration and Development 42, 56-65.

Hakimi, M.H., Abdullah, W.H., Sia, S.-G., Makeen, Y.M., 2013. Organic geochemical and petrographic characteristics of Tertiary coals in the northwest Sarawak, Malaysia: implications for palaeoenvironmental conditions and hydrocarbon generation potential. Marine and Petroleum Geology 48, 31-46.

Hameed, F., Khan, M.R., Dentith, M., 2023. Crustal study based on integrated geophysical techniques in the Northwestern Himalayas, Pakistan. Geological Journal n/a.

Hara, J., Tsuchiya, N., 2004. Coupled T (Thermal)-H (Hydrological)-C (Chemical) Process of Geothermal Alteration, Based On Experimental and Kinetic Considerations, Elsevier Geo-Engineering Book Series. Elsevier, pp. 655-660.

Hoentzsch, S., Scheibner, C., Brock, J.P., Kuss, J., 2013. Circum-Tethyan carbonate platform evolution during the Palaeogene: the Prebetic platform as a test for climatically controlled facies shifts. Turkish Journal of Earth Sciences 22, 891-918.

Jafarzadeh, M., Hosseini-Barzi, M., 2008. Petrography and geochemistry of Ahwaz Sandstone Member of Asmari Formation, Zagros, Iran: implications on provenance and tectonic setting. Revista mexicana de ciencias geológicas 25, 247-260.

Jafarzadeh M, N., Shoghani-Motlagh, M., Mousivand, F., Criniti, S., Critelli, S., 2022. Compositional and Geochemical Signatures of Oligocene volcanoclastic sandstones of Abbasabad-Kahak area, NE Iran: Implications for provenance relations and paleogeography. Marine and Petroleum Geology 139, 105605.

Jafarzadeh N, K., Ali, Bahrehvar, M., Wood, D.A., Janahmad, B., 2022. Reservoir characterization of fluvio-deltaic sandstone packages in the framework of depositional environment and diagenesis, the south Caspian Sea basin. Journal of Asian Earth Sciences 224, 105028.

Kadri, I.B., 1995. Petroleum geology of Pakistan. Pakistan Petroleum Limited.

Kalaitzidis, S., Siavalas, G., Skarpelis, N., Araujo, C.V., Christanis, K., 2010. Late Cretaceous coal overlying karstic bauxite deposits in the Parnassus-Ghiona Unit, Central Greece: Coal characteristics and depositional environment. International Journal of Coal Geology 81, 211-226.

Kazmi, A.H., Jan, M.Q., 1997. Geology and tectonics of Pakistan. Graphic publishers.

Kelemen, P., Dunkl, I., Csillag, G., Mindszenty, A., Józsa, S., Fodor, L., von Eynatten, H., 2022. Origin, timing and paleogeographic implications of Paleogene karst bauxites in the northern Transdanubian range, Hungary. International Journal of Earth Sciences, 1-22.

Khan, N., Ullah, W., Siyar, S.M., Wadood, B., Ayyub, T., Ullah, T., 2022a. Hydrocarbon source rock assessment of the shale and coal bearing horizons of the Early Paleocene Hangu Formation in Kala-Chitta Range, Northwest Pakistan. Journal of Petroleum Exploration and Production Technology, 1-18.

Khan, S.D., Walker, D.J., Hall, S.A., Burke, K.C., Shah, M.T., Stockli, L., 2009. Did the Kohistan-Ladakh island arc collide first with India? Geological Society of America Bulletin 121, 366-384.

Khan, S.H., Sheng, Y.-M., Mughal, M.S., Singh, B.P., Khan, M.R., Zhang, C., 2022b. Provenance of the Lower Cambrian Khewra Sandstone: Implications for Pan-African Orogeny. Sedimentary Geology 438, 106197.

Kiaeshkevarian, M., Calagari, A.A., Abedini, A., Shamanian, G., 2020. Geochemical and mineralogical features of karst bauxite deposits from the Alborz zone (Northern Iran): Implications for conditions of formation, behavior of trace and rare earth elements and parental affinity. Ore Geology Reviews 125, 103691.

Kreuzburg, M., Ibenthal, M., Janssen, M., Rehder, G., Voss, M., Naumann, M., Feldens, P., 2018. Sub-marine continuation of peat deposits from a coastal peatland in the southern baltic sea and its holocene development. Frontiers in Earth Science 6, 103.

Li, J., Hu, X., Garzanti, E., BouDagher-Fadel, M., 2022. Spatial heterogeneity in carbonate-platform environments and carbon isotope values across the Paleocene–Eocene thermal maximum (Tethys Himalaya, South Tibet). Global Planetary Change, 103853.

Li, S., Tian, J., Lin, X., Zuo, Y., Kang, H., Yang, D., 2020. Effect of alkaline diagenesis on sandstone reservoir quality: insights from the Lower Cretaceous Erlian Basin, China. Energy Exploration and Exploitation 38, 434-453.

Ling, K.-Y., Zhu, X.-Q., Tang, H.-S., Wang, Z.-G., Yan, H.-W., Han, T., Chen, W.-Y., 2015. Mineralogical characteristics of the karstic bauxite deposits in the Xiuwen ore belt, Central Guizhou Province, Southwest China. Ore Geology Reviews 65, 84-96.

Lorentzen, S., Augustsson, C., Nystuen, J.P., Berndt, J., Jahren, J., Schovsbo, N.H., 2018. Provenance and sedimentary processes controlling the formation of lower Cambrian quartz arenite along the southwestern margin of Baltica. Sedimentary Geology 375, 203-217.

Malekzadeh, M., Hosseini-Barzi, M., Sadeghi, A., Critelli, S., 2020. Geochemistry of Asara Shale member of Karaj Formation, Central Alborz, Iran: provenance, source weathering and tectonic setting. Marine and Petroleum Geology 121, 104584.

Malkani, M.S., Alyani, M.I., Khosa, M.H., 2016. New Fluorite and Celestite Deposits from Pakistan: Tectonic and Sedimentary Mineral Resources of Indus Basin (Pakistan)—An Overview. Lasbela University Journal of Science and Technology 5, 27-33.

Martín-Martín, M., Perri, F., Critelli, S., 2023. Cenozoic detrital suites from the Internal Betic-Rif Cordilleras (S Spain and N Morocco): implications for paleogeography and paleotectonics. Earth-Science Reviews 243, 104498.

McGowran, B., 2009. The Australo-Antarctic Gulf and the Auversian facies shift. Geological Society of America Special Papers 452, 215-240.

Meyer, F., 2004. Availability of bauxite reserves. Natural Resources Research 13, 161-172.

Mondillo, N., Herrington, R., Boni, M., 2021. Bauxites. Elsvier.

Montgomery, D.R., Zabowski, D., Ugolini, F.C., Hallberg, R.O., Spaltenstein, H., 2000. Soils, watershed processes, and marine. Earth System Science: From Biogeochemical Cycles to Global Changes 72, 159.

Mughal, M.S., Zhang, C., Du, D., Zhang, L., Mustafa, S., Hameed, F., Khan, M.R., Zaheer, M., Blaise, D.J.J.o.A.E.S., 2018. Petrography and provenance of the Early Miocene Murree Formation, Himalayan Foreland Basin, Muzaffarabad, Pakistan. 162, 25-40.

Munir, H., Baig, M.S., Mirza, K., 2006. Upper Cretaceous of Hazara and Paleogene Biostratigraphy of Azad Kashmir, North-West Himalayas, Pakistan. Geol. Bull. of Punjab. Univ, 40-41.

Nurhawaisyah, S., Jafar, N., Bakri, S., Artiningsih, A., Widodo, S., 2021. A petrographic study of bauxite of Kenco area, Landak District, West Kalimantan Province, IOP Conference Series: Earth and Environmental Science. IOP Publishing, p. 012048.

O'connor, G., Courtney, R., 2020. Constructed wetlands for the treatment of bauxite residue leachate: Long term field evidence and implications for management. Ecological Engineering 158, 106076.

Okolo, G.C., Emedo, O.C., Obumselu, A.C., Madukwe, F.C., Ulasi, A.N., 2020. Lithofacies, particle size analysis and paleodepositional environment of the Eze-Aku Group (Cenomanian–

Turonian) in the Itigidi-Ediba area, Afikpo Synclinorium, southeastern Nigeria. Journal of Sedimentary Environments 5, 375-398.

Okoro, A.U., Igwe, E.O., Umo, I.A., 2020. Sedimentary facies, paleoenvironments and reservoir potential of the Afikpo Sandstone on Macgregor Hill area in the Afikpo Sub-basin, southeastern Nigeria. Applied Sciences 2, 1-17.

Oye, O.J., Aplin, A.C., Jones, S.J., Gluyas, J.G., Bowen, L., Harwood, J., Orland, I.J., Valley, J.W., 2020. Vertical effective stress and temperature as controls of quartz cementation in sandstones: Evidence from North Sea Fulmar and Gulf of Mexico Wilcox sandstones. Marine and Petroleum Geology 115, 104289.

Pazand, K., Aghaei Kerigh, M., Rezvanianzadeh, M.R., 2021. Geology, petrography, alteration, and geochemistry of the Shahrab igneous rock, Central Iran. Geology, Ecology, and Landscapes, 1-10.

Perri, F., Cirrincione, R., Critelli, S., Mazzoleni, P., Pappalardo, A., 2008. Clay mineral assemblages and sandstone compositions of the Mesozoic Longobucco Group, northeastern Calabria: implications for burial history and diagenetic evolution. International Geology Review 50, 1116-1131.

Qasim, M., Khan, M.A., Haneef, M., 2014. Stratigraphic characterization of the Early Cambrian Abbottabad Formation in the Sherwan area, Hazara region, N. Pakistan: Implications for Early Paleozoic stratigraphic correlation in NW Himalayas, Pakistan. Journal of Himalayan Earth Science 47.

Qureshi, K.A., Shah, M.R., Meerani, I.A., Fahad, S., Hussain, H., Habib, U., 2020. Sedimentology and economic significance of Hangu formation, Northwest Pakistan. International Journal of Economic and Environmental Geology 11, 48-55.

Ramadhan, F.R., Aribowo, Y., Widiarso, D.A., Betraz, A., 2014. Geologi, Karakteristik dan Genesa Endapan Laterit Bauksit PT. Antam (Persero) Tbk, Unit Geomin, Daerah Kenco, Kabupaten Landak, Provinsi Kalimantan Barat. Geological Engineering E-Journal 6, 80-95.

Ramanaidou, E., 2009. Genesis of lateritic iron ore from banded iron-formation in the Capanema mine (Minas Gerais, Brazil). Australian Journal of Earth Sciences 56, 605-620.

Scarciglia, F., Le Pera, E., Critelli, S., 2007. The onset of the sedimentary cycle in a mid-latitude upland environment: weathering, pedogenesis, and geomorphic processes on plutonic rocks (Sila Massif, Calabria).

Scarciglia, F., Le Pera, E., Vecchio, G., Critelli, S., 2005. The interplay of geomorphic processes and soil development in an upland environment, Calabria, South Italy. Geomorphology 69, 169-190.

Schulte, R.F., Foley, N.K., 2014. Compilation of gallium resource data for bauxite deposits. US Department of the Interior, US Geological Survey.

Seraine, M., Campos, J.E.G., Martins-Ferreira, M.A.C., Giorgioni, M., Angelo, T.V., 2020. Tectonic significance of abrupt immature sedimentation in a shallow cratonic margin basin: The Arkose Level, Mesoproterozoic Paranoá Group. Journal of South American Earth Sciences 97, 102397.

Shah, S.J.T.G.S.o.P., 2009. Stratigraphy of Pakistan (memoirs of the geological survey of Pakistan). 22.

Sidibe, M., Yalcin, M.G., 2019. Petrography, mineralogy, geochemistry and genesis of the Balaya bauxite deposits in Kindia region, Maritime Guinea, West Africa. Journal of African Earth Sciences 149, 348-366.

Singh, P.K., Khan, M.S., 2017. Geochemistry of Palaeoproterozoic rocks of Aravalli Supergroup: implications for weathering history and depositional sequence. International Journal of Geosciences 8, 1278-1299.

Sun, L., Zhang, S., Zhang, S., Liu, J., Xiao, K., 2020. Geologic characteristics and potential of bauxite in China. Ore Geology Reviews 120, 103278.

Sunderlin, D., Trop, J.M., Idleman, B.D., Brannick, A., White, J.G., Grande, L., 2014. Paleoenvironment and paleoecology of a late Paleocene high-latitude terrestrial succession, Arkose Ridge Formation at Box Canyon, southern Talkeetna Mountains, Alaska. Palaeogeography, Palaeoclimatology, Palaeoecology 401, 57-80.

Suttner, L.J., Dutta, P.K.J.J.o.S.R., 1986. Alluvial sandstone composition and paleoclimate; I, Framework mineralogy. 56, 329-345.

Ueki, K., Iwamori, H., 2017. Geochemical differentiation processes for arc magma of the Sengan volcanic cluster, Northeastern Japan, constrained from principal component analysis. Lithos 290, 60-75.

Ullah, M.F., Mahmood, K., Akram, M.S., 2018. Coal mining trends and future prospects: A case study of Eastern Salt Range, Punjab, Pakistan. Journal of Himalayan Earth Science 51.

Ullah, Z., Li, J.-W., Robinson, P.T., Wu, W.-W., Khan, A., Dac, N.X., Adam, M.M.A., 2020a. Mineralogy and geochemistry of peridotites and chromitites in the Jijal Complex ophiolite along the Main Mantle Thrust (MMT or Indus Suture Zone) North Pakistan. Lithos 366, 105566.

Ullah, Z., Shah, M.T., Siddiqui, R.H., Lian, D.-Y., Khan, A., 2020b. Petrochemistry of high-Cr and high-Al chromitites occurrences of dargai complex along indus suture zone, northern Pakistan. Episodes Journal of International Geoscience 43, 689-709.

Van De Kamp, P.C., 2010. Arkose, subarkose, quartz sand, and associated muds derived from felsic plutonic rocks in glacial to tropical humid climates. Journal of Sedimentary Research 80, 895-918.

Violante, A., Ricciardella, M., Pigna, M., Capasso, R., 2005. Effects of organic ligands on the adsorption of trace elements onto metal oxides and organo-mineral complexes, Biogeochemistry of trace elements in the rhizosphere. Elsevier, pp. 157-182.

Wang, J.-G., Hu, X.-M., BouDagher-Fadel, M., Wu, F.-Y., Sun, G.-Y., 2015. Early Eocene sedimentary recycling in the Kailas area, southwestern Tibet: Implications for the initial India–Asia collision. Sedimentary Geology 315, 1-13.

Wang, W., Cawood, P.A., Pandit, M.K., Xia, X., Raveggi, M., Zhao, J., Zheng, J., Qi, L., 2021. Fragmentation of South China from greater India during the Rodinia-Gondwana transition. Geology 49, 228-232.

Wang, X., Chen, T., Xu, H., 2020. Thickness distribution prediction for tectonically deformed coal with a deep belief network: a case study. Energies 13, 1169.

Warwick, P.D., Javed, S., Mashhadi, S.T.A., Shakoor, T., Khan, A.M., Khan, A.L., 1995. Lithofacies and palynostratigraphy of some Cretaceous and Paleocene rocks, Surghar and Salt Range coal fields, northern Pakistan. US Government Printing Office.

Yang, L., Wang, Q., Zhang, Q., Carranza, E.J.M., Liu, H., Liu, X., Deng, J., 2017a. Interaction between karst terrain and bauxites: evidence from Quaternary orebody distribution in Guangxi, SW China. Scientific reports 7, 11842.

Yang, L., Wang, Q., Zhang, Q., Carranza, E.J.M., Liu, H., Liu, X., Deng, J.J.S.r., 2017b. Interaction between karst terrain and bauxites: evidence from Quaternary orebody distribution in Guangxi, SW China. 7, 11842.

Yang, R., van Loon, A.T., Jin, X., Jin, Z., Han, Z., Fan, A., Liu, Q., 2019. From divergent to convergent plates: Resulting facies shifts along the southern and western margins of the Sino-Korean Plate during the Ordovician. Journal of Geodynamics 129, 149-161.

Yang, S., Wang, Q., Liu, X., Kan, Z., Santosh, M., Deng, J., 2022. Global spatio-temporal variations and metallogenic diversity of karst bauxites and their tectonic, paleogeographic and paleoclimatic relationship with the Tethyan realm evolution. Earth-Science Reviews, 104184.

Yaseen, M., Naseem, A.A., Ahmad, J., Mehmood, M., Anjum, M.N., 2021. Integrated approach for inventories and quantitative assessment of geological and paleontological sites from Precambrian to quaternary successions in the Salt Range, Pakistan. Geoheritage 13, 31.

Zaheer, M., Khan, M.R., Mughal, M.S., Janjuhah, H.T., Makri, P., Kontakiotis, G., 2022. Petrography and Lithofacies of the Siwalik Group in the Core of Hazara-Kashmir Syntaxis: Implications for Middle Stage Himalayan Orogeny and Paleoclimatic Conditions. Minerals 12, 1055.

Table 1 Mineralogical composition of studied bauxite deposits. The minerals are sorted according to their economic value. Sample numbers HB1–2 represent karst, while HB3–6 represent lateritic bauxite.

Distance from base	Sample no.	Gibbsite	Diaspore (%)	Goethite vein (%)	Biotite (%)	Hematite vein (%)	Hematite cement (%)	Kaolinite (%)
84 cm	HB6	34	-	5	1	-	37	23
72 cm	HB5	33	-	6	2	1	38	20
48 cm	HB4	31	4	-	-	-	45	20
36 cm	HB3	30	5	-	-	-	47	18
4 cm	HB2	3	25	-		4	52	16
2 cm	HB1	2	28	-	-	5	50	15

Table 2 Mineralogical composition of the Hangu Formation sandstone. Metam., Metamorphic; Sedim., Sedimentary; Limest., Limeston

Sample No.			YH 1	YH 2	YH 3	YH 4	YH 5	YH 6	YH 7	YH 8	YH 9	YH 10	YH 11	YH 12	YH 13	YH 14	YH 15	YH 16	YH 17	YH 18	YH 19	YH 20	YH 21	YH 22	YH 23
Above from base-top of each facies, respectively			equal interval of 15 cm										equal interval of 9 cm								equal interval of 30 cm				
Facies			Sub-arkose (Sf_1)										Arenite (Sf_2)								Arkose (Sf_3)				
Quartz	Poly	>3 grains	62	61	60	65	64	44	45	72	70	73	75	74	8	10	44	40	5	8	30	40	27	30	28
	Mono	Qnu	-	-	-	-	-	40	38	-	-	-	-	-	77	73	25	30	78	79	18	22	37	35	35
		Qu	-	-	-	-	-	-	-	-	-	-	-	-	-	-	-	-	-	-	-	-	5	-	-
Feldspar	Plagioclase		1		1	-	-	-	-	-	-	-	-	-	-	-	-	-	-	1	2	1	1	2	2
	Perthite		1		1	1	1		-	-	-	-	-	-	-	-	-	-	-	1	5	4	3	4	5
	Orthoclase		6	6	7	6	7	5	4	5	5	5	4	3	3	2	3	3	2	1	15	16	13	17	18
Rock fragments	Igneous	Basalt	-	-	-	-	-	-	-	-	-	-	-	-	-	-	-	-	-	-	1	1	-	-	-
	Metam.	Chert	-	-	-	-	-	-	-	-	-	-	-	-	-	-	-	-	1	1	-	-	-	-	-
	Sedim.	Limest.	-	-	-	-	-	-	-	-	-	-	-	-	-	-	-	-	-	-	1	1	-	1	-
Accessory minerals	Rutile		1	1	1	1	1	-	-	-	-	-	-	-	-	-	1	1	-	-	-	-	-	-	-
	Tourmaline		1	1	1	1	1	1	1	1	1	1	1	1	1	1	1	1	-	-	-	-	-	-	-
	Apatite		-	-	-	-	-	-	-	-	-	-	-	-	-	-	-	-	-	-	1	1		1	
	Zircon		1	1	1	1	1	1	1	1	1	1	1	1	1	1	-	-	1	1	1	1		1	
	Hematite		-	-	-	-	-	-	-	-	-	-	-	-			-	-	-	-	3	4	2	1	2
	Muscovite		-	-	-	-	-	-	-	-	-	-	-	-	1	1	-	-	-	-	-	-			
	Biotite		-	-	-	-	-	-	-	-	-	-	-	-	1	1	-	-	-	-	-	-	1	1	1
	Chlorite		-	-	-	-	-	-	-	-	-	-	-	-	1	1	-	-	-	-	-	-	-	-	-
	Garnet		-	-	-	-	-	-	-	-	-	-	-	-	-	-	-	-	1	1	-	-	-	-	-
	Sericite		1	1	1	1	1	1	1	1	1	1	1	1	-	-	2	2	1	1	2	1	-	-	-
	Pyrite		-	-	-	-	-	-	-	-	-	-	-	-	-	-	-	-	1	-	1	1	1	1	1
Cementing material	Calcite		-	-	-	-	-	-	-	-	-	-	-	-	-	-	-	-	-	-	1	1	-	-	-
	Sillica		14	16	15	13	15	3	4	20	22	19	18	20	2	3	8	6	2	1	2	2	2	1	1
	Hematite		5	5	4	4	3	2	2	-	-	-	-	-	5	7	10	8	5	4	3	4	5		3
	Dolomite		-	-	-	-	-	-	-	-	-	-	-	-	-	-	1	1	-	-	-	-	-	-	-
Matrix	Clay		-	-	-	-	-	-	-	-	-	-	-	-	-	-	-	-	-	-	-	-	2	2	3
	Hematite vein		2	2	1	2	2	3	4	-	-	-	-	-	-	-	5	8	-	-	4	-	1	3	1
	Calcite grain		-	-	-	-	-	-	-	-	-	-	-	-	-	-	-	-	1	1	-	-	-	-	-
	Chert vein		5	6	6	5	4	-	-	-	-	-	-	-	-	-	-	-	-	-	-	-	-	-	-
Total (%)			100	100	100	100	100	100	100	100	100	100	100	100	100	100	100	100	100	100	100	100	100	100	100

Table 3 Recalculated sandstone detritus of the Hangu Formation.

Sample no.	Facies	QtFL%			QmFLt%			QmPK%			QtF%	
		Qt	F	L	Qm	F	Lt	Qm	P	K	Qt	F
MH1	Arkose	91.1	11.7	0	0	8	62	0	1	7	88	12
MH2		91	9.8	0	0	6	61	0	0	6	91	9
MH3		86.9	13	0	0	9	60	0	1	8	87	13
MH4		90.2	9.7	0	0	7	65	0	0	7	90	10
MH5		88.8	11.1	0	0	8	64	0	0	8	89	11
MH6		94.3	5.6	0	40	5	44	40	0	5	94	6
MH7		95.4	4.5	0	38	4	45	38	0	4	94	6
MH8		93.5	6.5	0	0	5	72	0	0	5	93	7
MH9		93.3	6.6	0	0	5	70	0	0	5	93	7
MH10		93.5	6.4	0	0	5	73	0	0	5	94	6
MH11	Arenite	95	5	0	0	4	75	0	0	4	95	5
MH12		96.1	3.8	0	0	3	74	0	0	3	96	4
MH13		96.5	3.4	0	77	3	8	77	0	3	97	3
MH14		97.6	2.3	0	73	2	10	73	0	2	98	2
MH15		95.8	4.1	0	25	3	44	25	0	3	96	4
MH16		95.8	4.1	0	30	3	40	30	0	3	96	4
MH17		94.3	4.5	0.1	78	4	6	78	1	3	95	5
MH18		95.6	3.2	0.1	79	3	9	79	1	2	97	3
MH19	Sub-arkose	66.6	30.5	1.3	18	22	32	18	2	20	68	2
MH20		72.9	24.7	2.3	22	21	42	22	1	20	75	25
MH21		74.4	25.5	0	37	22	27	37	1	16	74	26
MH22		73	25.8	1.1	35	23	31	35	2	21	74	26
MH23		71.5	28.4	0	35	25	28	35	2	23	71	29
Means		88.8	10.0	0.2	25.5	8.7	45.3	25.5	0.5	7.9	88.9	9.8
Standard Deviation		9.42	3.3	0.5	5.0	2.9	6.7	5.0	0.7	2.8	9.4	3.1

Table 4. Mineralogical composition of the thin sections from limestone facies.

Distance from base of bed	Sample no.	Micrite (%)	Bioc-lasts (%)	C.M (%)	Pyrite (%)	Hema-tite (%)	Calcite (%)	Quartz (%)	Dunham classificati-on
10 cm	YH5	80	2	2	2	7	6	1	Mudstone
8 cm	YH4	79	1	3	1	8	5	1	
6 cm	YH3	80	3	3	1	6	6	1	
4 cm	YH2	78	2	2	2	8	7	1	
2 cm	YH1	79	3	2	2	7	6	1	

Table 5. Stratigraphic sequences in the different areas of the Indus Basin (IB) (modified after (Bilal et al., 2023).

System/ Period	Series/ Epoch/Stage	Core of HKS (This study)	EL of HKS Bilal et al., 2023	Upper Indus Basin Bilal et al., 2022	Middle Indus Basin	Lower Indus Basin
Quaternary	Holocene Pleistocene	Alluvium Mirpur Conglomerate	Alluvium	Alluvium Lei Conglomerate	Alluvium Lei Conglomerate	Alluvium Lei Conglomerate
Neogene	Pliocene	Soan Fm. Dhoke Pathan Fm.		Soan Fm. Dhoke Pathan Fm.	Soan Fm. Dhoke Pathan Fm.	Soan Fm. Dhoke Pathan Fm.
	Miocene	Nagri Fm. Chingi Fm. Kamlial Fm. Murree Fm.	Murree Fm.	Nagri Fm. Chingi Fm. Kamlial Fm. Murree Fm.	Nagri Fm. Chingi Fm.	Nagri Fm. Chingi Fm. Gaj Fm.
Paleogene	Oligocene					Nari Fm.
	Eocene	Kuldana Fm. Chorgali Fm. Margala Hill Limestone	Kuldana Fm.	Kuldana Fm. Chorgali Fm. Sakesar Limestone Nammal Fm. Margala Hill Limestone	Kirthar Fm. Ghazij Group Laki/Sui Main Limestone	Kirthar Fm. Ghazij Group Laki/Sui Main Limestone
	Paleocene: Thanetian	Patala Fm. Lockhart Limestone	Patala Fm. Lockhart Limestone	Patala Fm. Lockhart Limestone.	Ranikot Fm.	Ranikot Fm.
	Paleocene: Selandian Danian	Hangu Fm.		Hangu Fm.		
Cretaceous	Upper			Kawagarh Fm.	Pab Sandstone Fort Munro Fm. Mughalkot Fm.	Pab Sandstone Fort Munro Fm. Mughalkot Fm.
	Lower			Lumshiwal Fm. Chichali Fm.	Par Limestone Goru Fm. Sember Fm.	Par Limestone Goru Fm. Sember Fm.
Jurassic	Upper Lower			Samanasuk Fm. Shinwari Fm. Datta Fm.	Chiltan Fm.	Chiltan Fm. Shirinab Fm.
Triassic	Upper Middle Lower			Kingriali Fm. Tredian Fm. Mianwali Fm.	Wulgai Fm.	Wulgai Fm.
Permian	Lopingian		Panjal Fm.	Chidru Fm. Wargal Limestone Amb Fm. Sardhai Fm. Warcha Sandstone Dandot Fm. Tobra Fm.	Not exposed or drilled	Not exposed or drilled
	Cisuralian					
Carbonif-erous			Gondwana Group			
Devonian	Upper Lower					
Silurian						
Ordovician						
Cambrian	Furongian Miaolingian Series 2	Abbottabad Fm.	Kailar Fm.	Baghanwala Fm. Jutana Fm. Kussak Fm. Khewra sandstone		
Pre-cambrian	Proterozoic	Hazara Fm. / Dogra Slates	Hazara Fm. / Dogra Slates	Salt range Fm. Crystalline Bascement		

Table 6 Facies descriptions and their interpretations.

Lithology	**Field results**	**Petrographic results**	**Facies**	**Sedimentary environment**	**Paleo-climate**
Limestone	Limestone lenses	Micritic mudstone	Lf_1	Shallow marine carbonate platform	Humid near-coast brackish regions
Coal II	Medium bedded	-	C_2	Peat land, river/sea catchments	Humid–Tropical
Sandstone III	Medium bedded, coarse-grained, highly ferruginous, very hard	Arkose	Sf_3	High-energy river channel-fluvial	Arid to semi-arid
Sandstone II	Medium bedded, coarse-grained, very hard	Arenite	Sf_2	Constant high energy, coastal and nearshore	Humid to hot-humid
Sandstone I	Hard but highly fractured (blocky), coarse-grained	Sub-Arkose	Sf_1	Transitional continental/ deltaic environment	Sub-humid
Coal I	1 cm thick lamina	-	C_1	Failed peat land, river catchments	Humid–Tropical
Bauxite II	Black fireclay rock	Gibbsite dominant	B_2	Intense chemical weathering of overlying lateritic deposits on carbonate platform	Intense Humid
Bauxite I	Fine black powdered	Diaspore dominant	B_1	Intense chemical weathering of overlying deposits above Karst and platform landscape	Humid

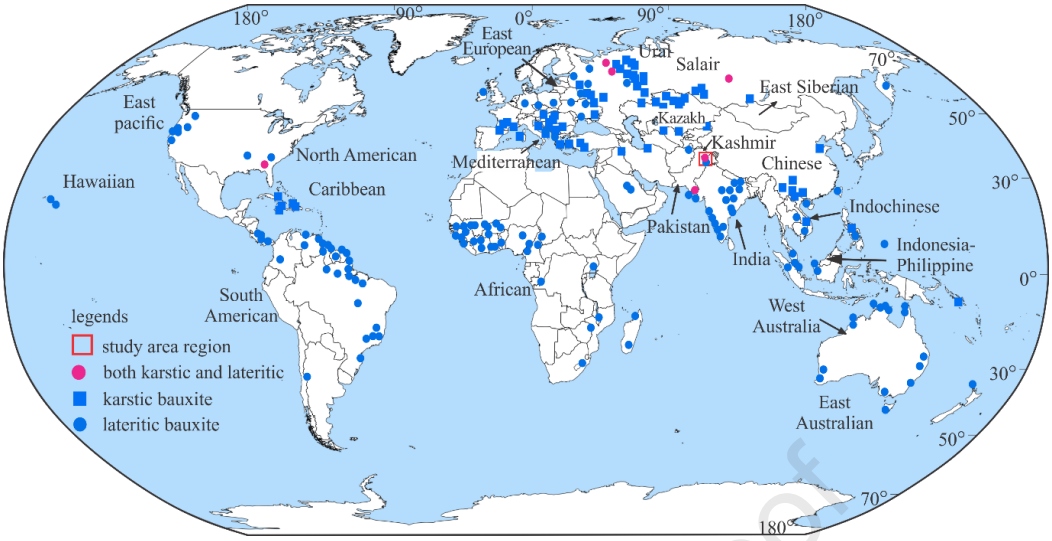

Fig. 1. Global distribution of karst and lateritic bauxite and the location of the study region (modified after (Schulte and Foley, 2014).

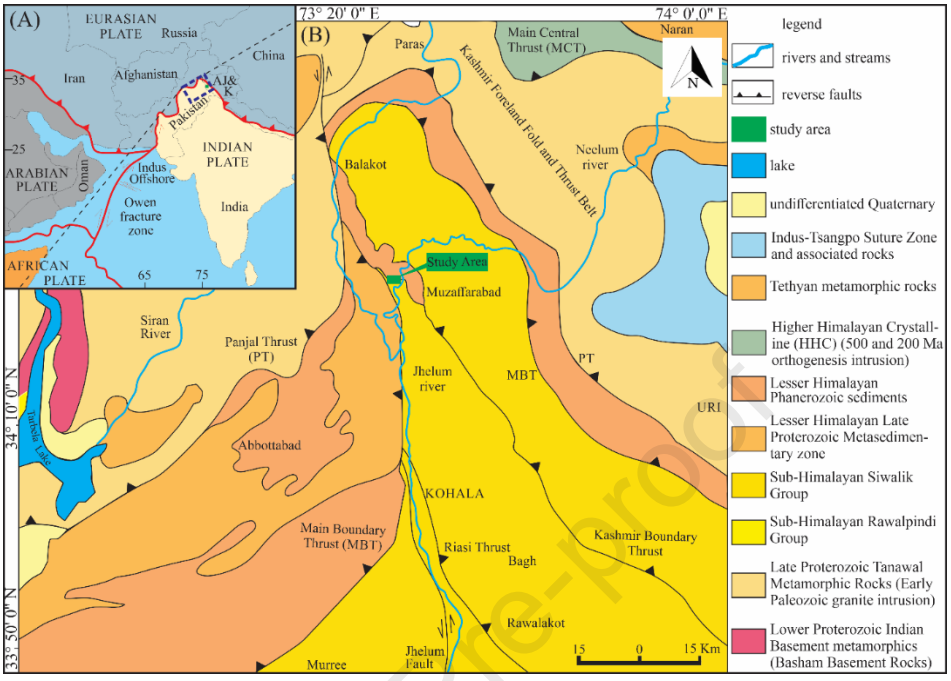

Fig. 2. (A) A regional tectonic model and the location of the study area; (B) the tectono-sedimentary setting of the Hazara Kashmir Syntaxis (HKS) (modified after (Bilal et al., 2022b).

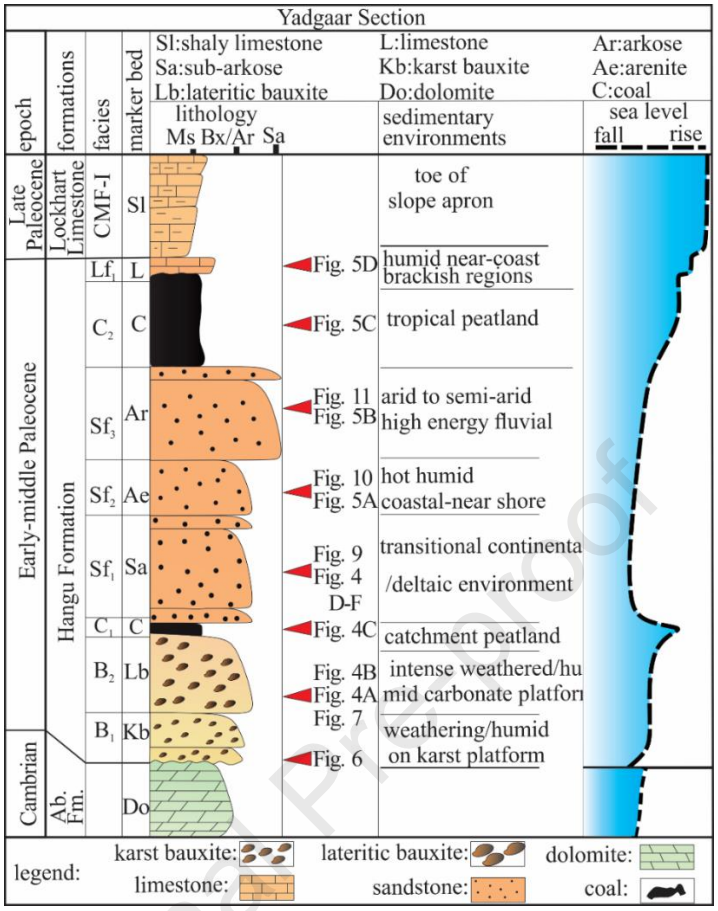

Fig. 3. (A) The lithology, sedimentary environments, and facies of the Yadgaar Section.

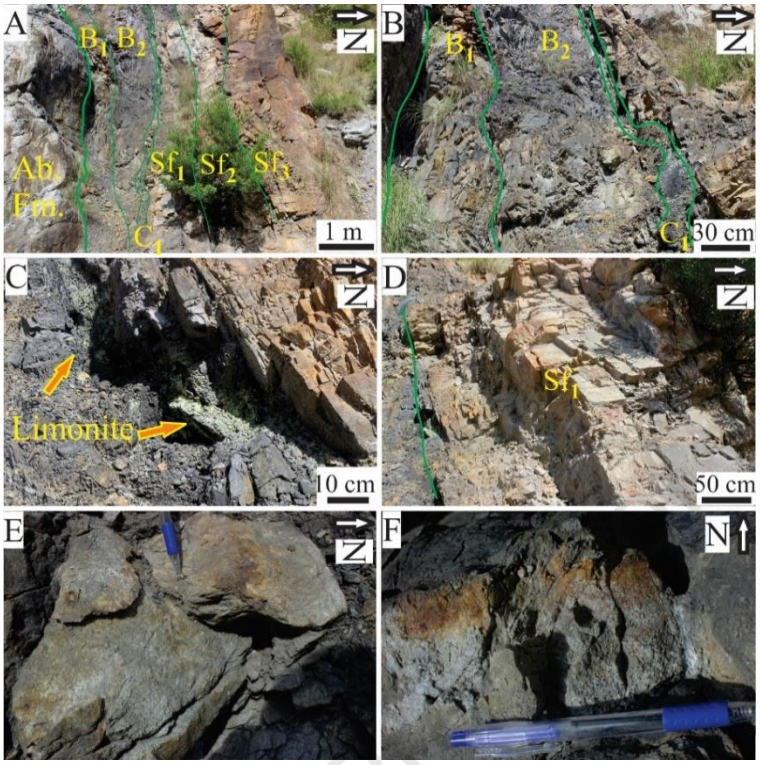

Fig. 4. Field images of the Hangu Formation facies suit. (A) the unconformable lower contact with Abbottabad Formation (Ab. Fm.: Abbottabad Formation; B_1: Bauxite layer 1; B_2: Bauxite layer 2; C_1: Coal layer 1; Sf_1: Sandstone facies 1); (B) bauxite and coal strata; (C) limonite from the sandstone leaching onto the lower coal deposit; (D) sub-Arkose sandstone beds; (E) and (F) coarse-graines sub-arkose sandstone (length of the blue cap of the pen is 2.5 cm). For abbreviations, please see Fig. 3.

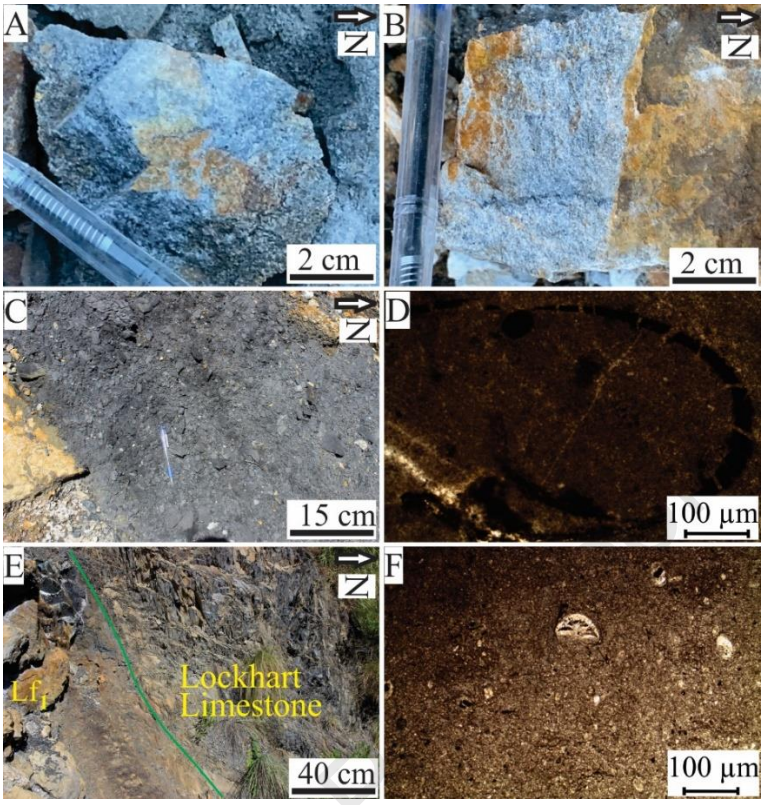

Fig. 5. Field images of the Hangu Formation facies suit. (A) arenite facies; (B) arkose facies; (C) coal facies; (D) framboidal pyrite transitioning into hematite, which further replaces bioclasts in the micrite matrix (PPL); (E) limestone facies with upper contact to the overlying Lockhart Limestone; (F) green algae fossils that are partially micritized due to diagenesis (Bilal et al., 2022a) (PPL).

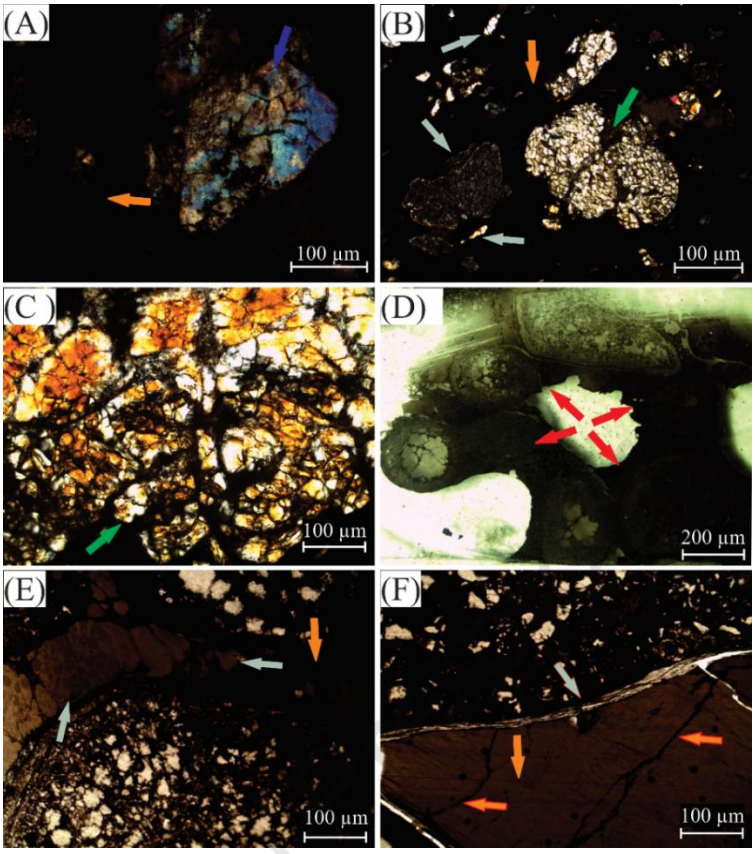

Fig. 6. Photomicrographs of the karst bauxite thin sections of (HB1– HB3): (A) diaspore and hematite (X-PL); (B) fractured quartz, hematite, and kaolinite (X-PL); (C) fractured quartz with fractures filled with hematite cement (X-PL); (D) gibbsite grains (PPL); (E) kaolinite and hematite (X-PL); (F) older hematite veins are cut by younger kaolinite veins (X-PL). The arrows denote the following minerals: dark blue: diaspore; brown: hematite; green: fracture quartzite; sky blue: kaolinite; sky blue arrows with red outline: kaolinite vein; red: gibbsite; brown arrows with red outlines: hematite veins.

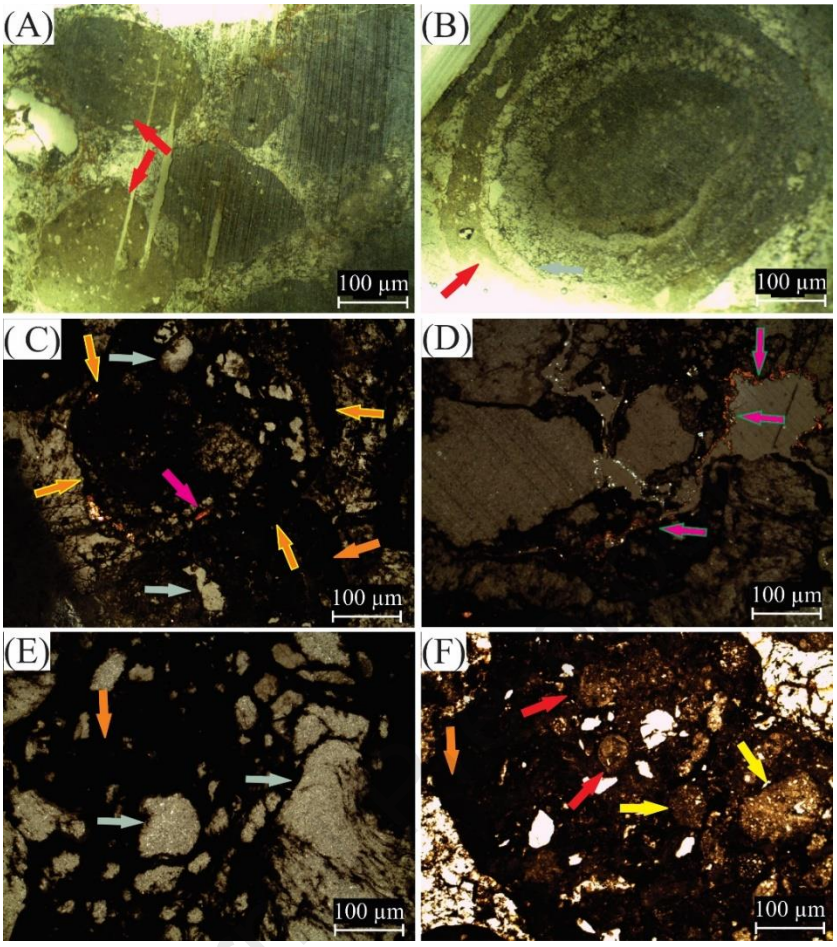

Fig. 7. Photomicrographs of the lateritic bauxite thin sections of (HB4–HB6): (A-B) gibbsite grains (PPL); (C) lateritic circular hematite and kaolinite (X-PL); (D) goethite veins (X-PL); (E) hematite and kaolinite (X-PL); (F) gibbsite, hematite, and limestone clasts (X-PL). The arrows denote the following minerals: brown arrows with yellow outlines: lateritic circular hematite; purple: goethite; purple arrows with green outlines: goethite veins; yellow: limestone clasts. See figure caption of Fig. 3 for additional arrow colors.

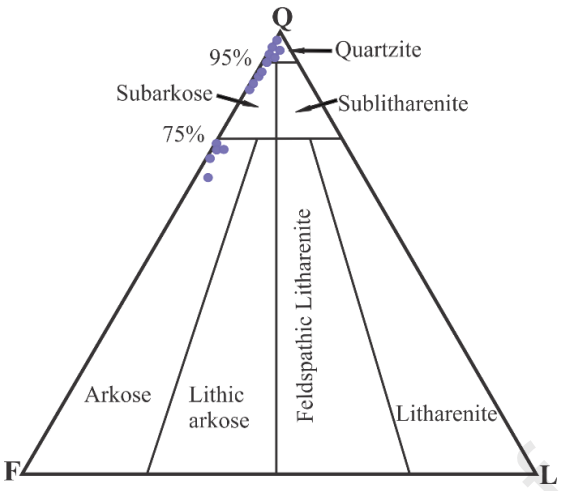

Fig. 8. Mineralogical classification of the sandstones of the Hangu Formation on a QFL diagram (Folk, 1968).

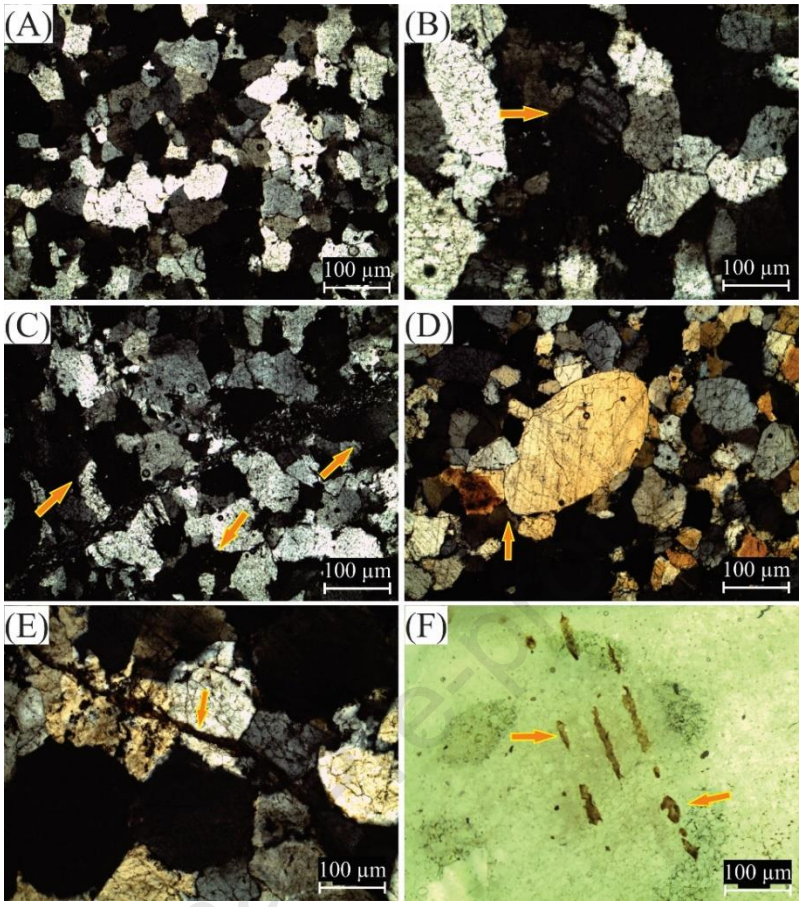

Fig. 9. Photomicrographs of the sub-arkose thin sections of Sf_1: (A) close packing of polycrystalline quartz (X-PL); (B) plagioclase grain (X-PL); (C) orthoclase grains (X-PL); (D) detrital rounded quartz grain (X-PL); (E) hematite vein (X-PL); (F) parallel leaching of hematite (PPL).

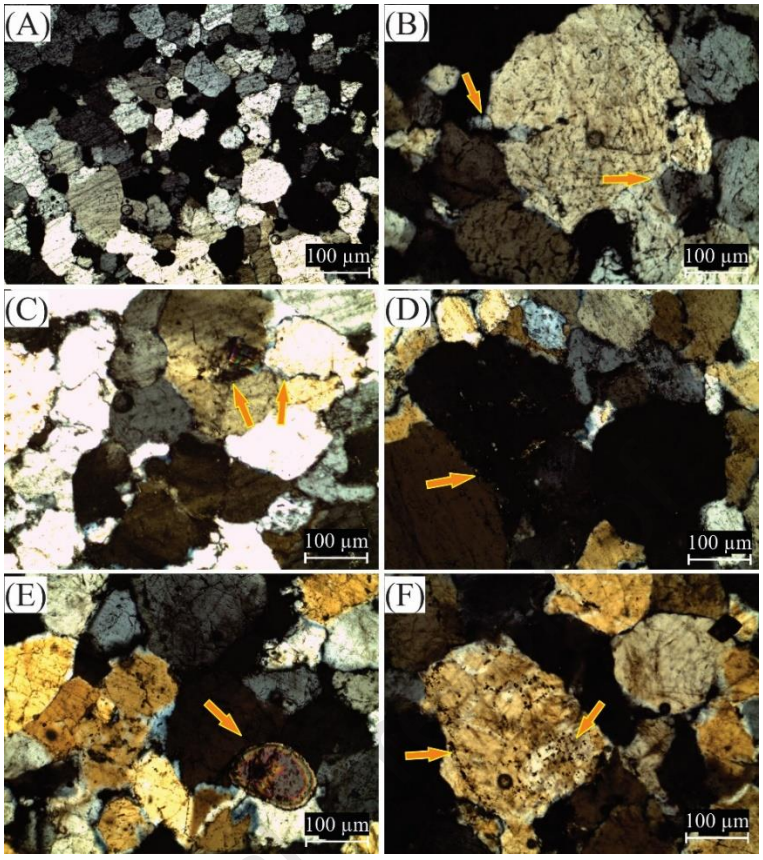

Fig. 10. Textures and mineral content in the quartz-arenite sf_2: (A) close packing of the quartz grains; (B) dissolved quartz boundaries and silica cement; (C) alteration of biotite into muscovite and further change into chlorite; (D) alteration of orthoclase into sericite; (E) tourmaline grain; (F) pyrite grain and inclusion of igneous zircon in quartz.

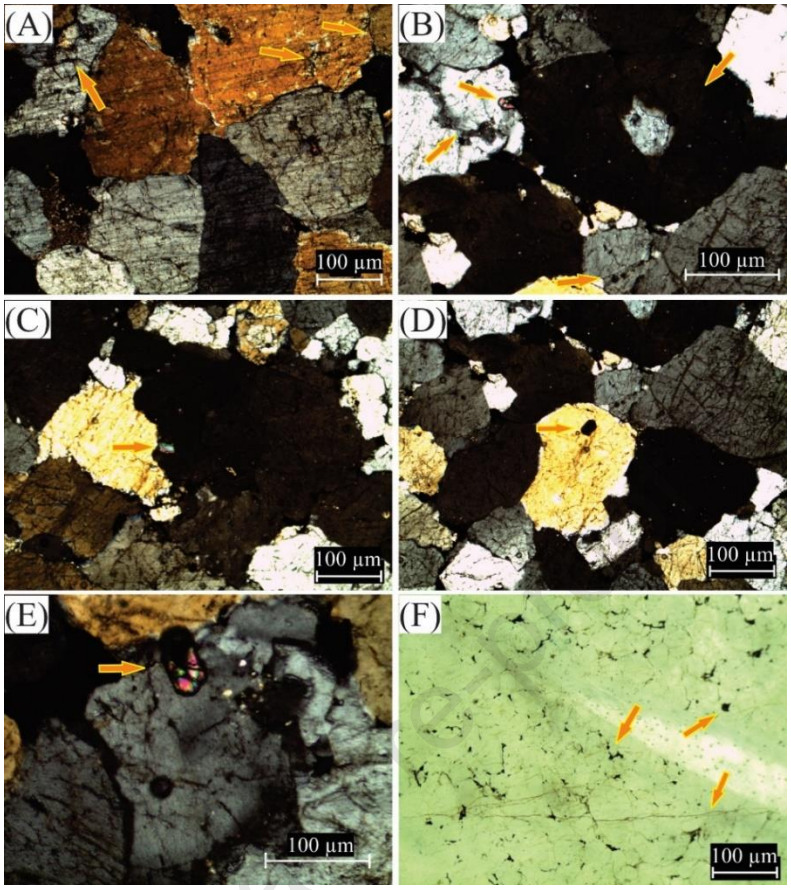

Fig. 11. Texture and mineral content of the studied arkose samples sf_3: (A) large quartz grains; (B) K-feldspar (orthoclase) being altered to sericite; (C) perthite alteration into sericite and muscovite; (D) an opaque phase of zircon; (E) zircon inclusion in quartz; (F) hematite cement.

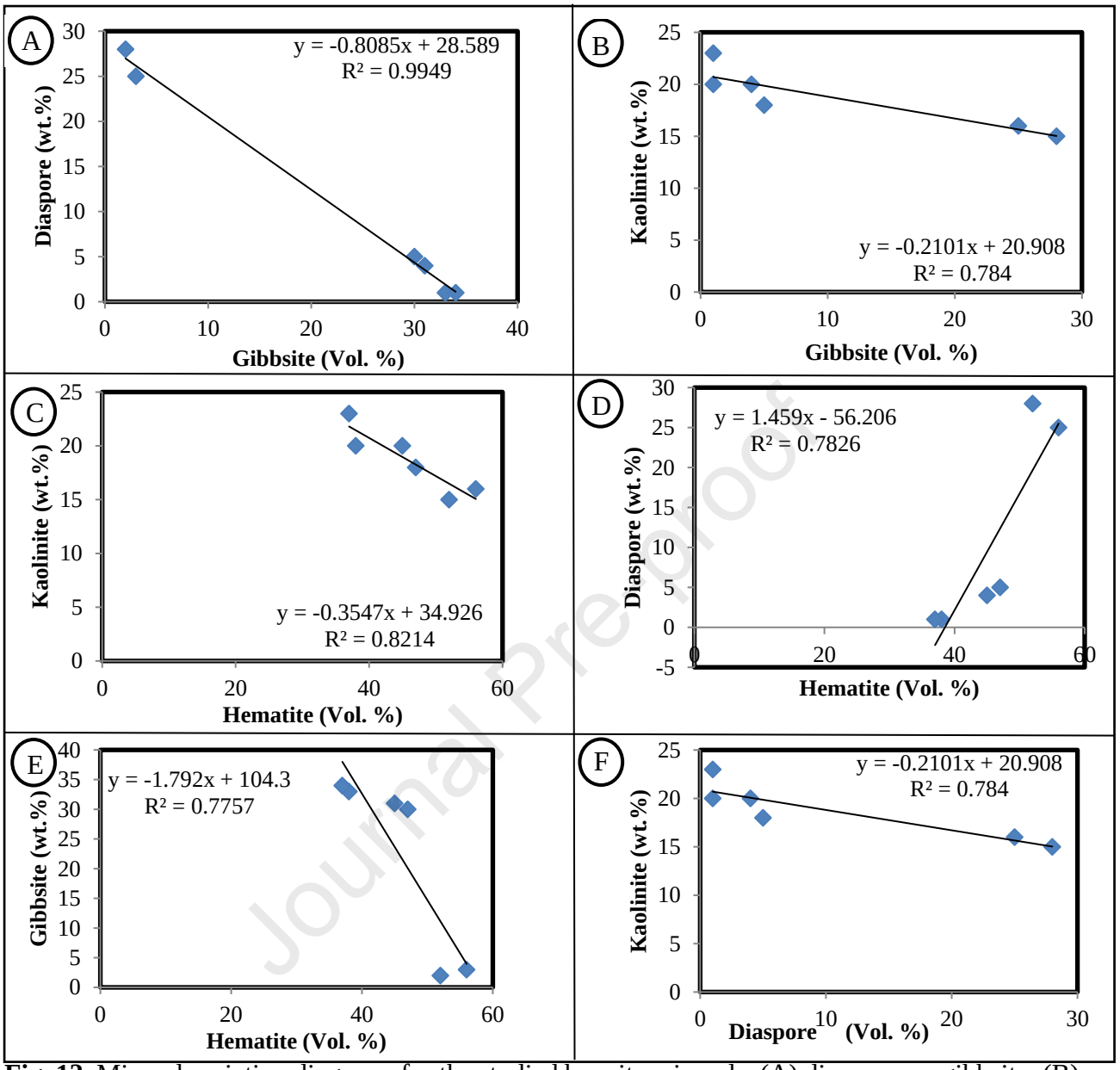

Fig. 12. Mineral variation diagrams for the studied bauxite minerals. (A) diaspore vs. gibbsite; (B) kaolinite vs. gibbsite; (C) kaolinite vs. hematite; (D) diaspore vs. hematite; (E) gibbsite vs. hematite; (F) kaolinite vs. diaspore.

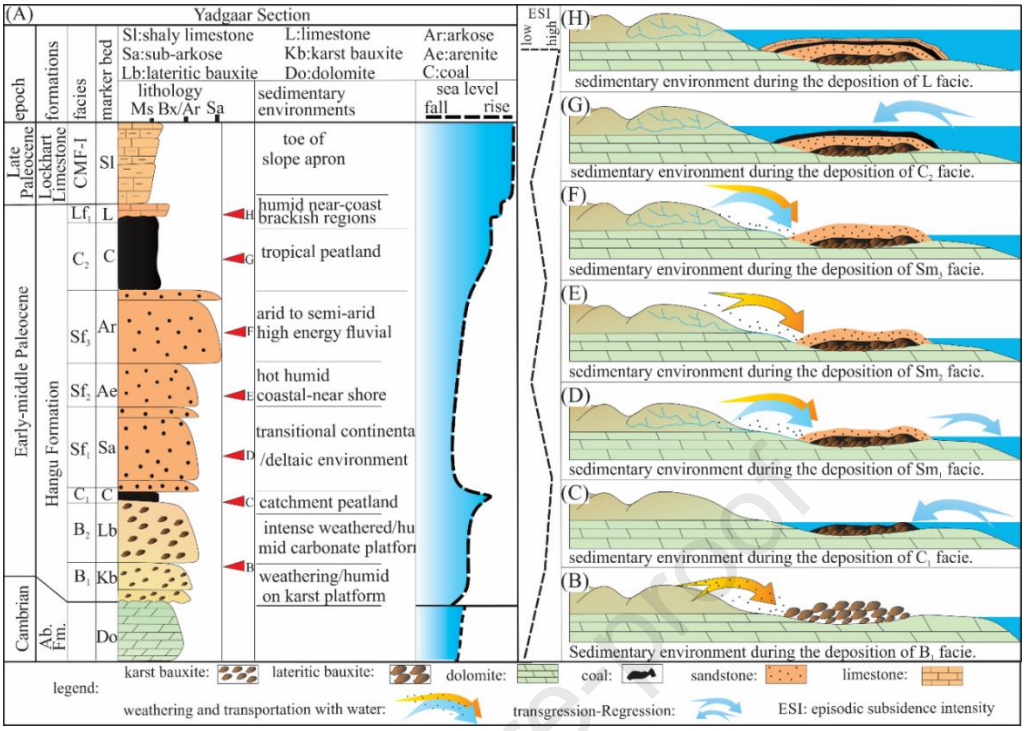

Fig. 13. (A) Histogram of the Hangu Formation profile; (B–H) evolution of the topology in response to tectonic events, sedimentary environment and facies shift during the deposition of the facies suit.

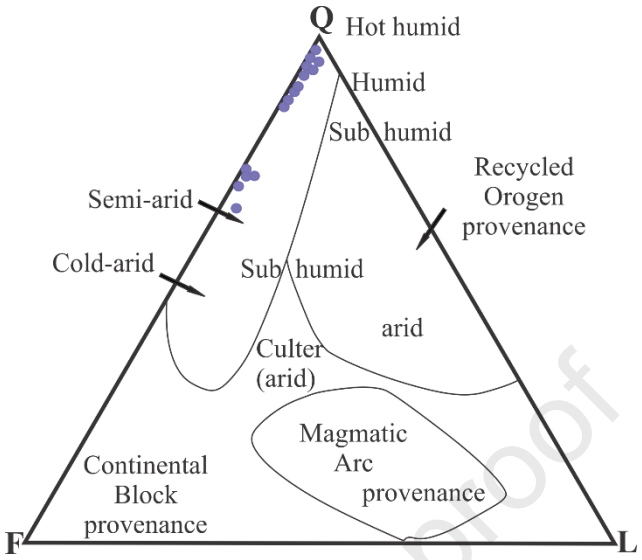

Fig. 14. Paleoclimatic interpretation from the QFL ternary diagram for the sandstones of the Hangu Formation (based on (Suttner and Dutta, 1986).

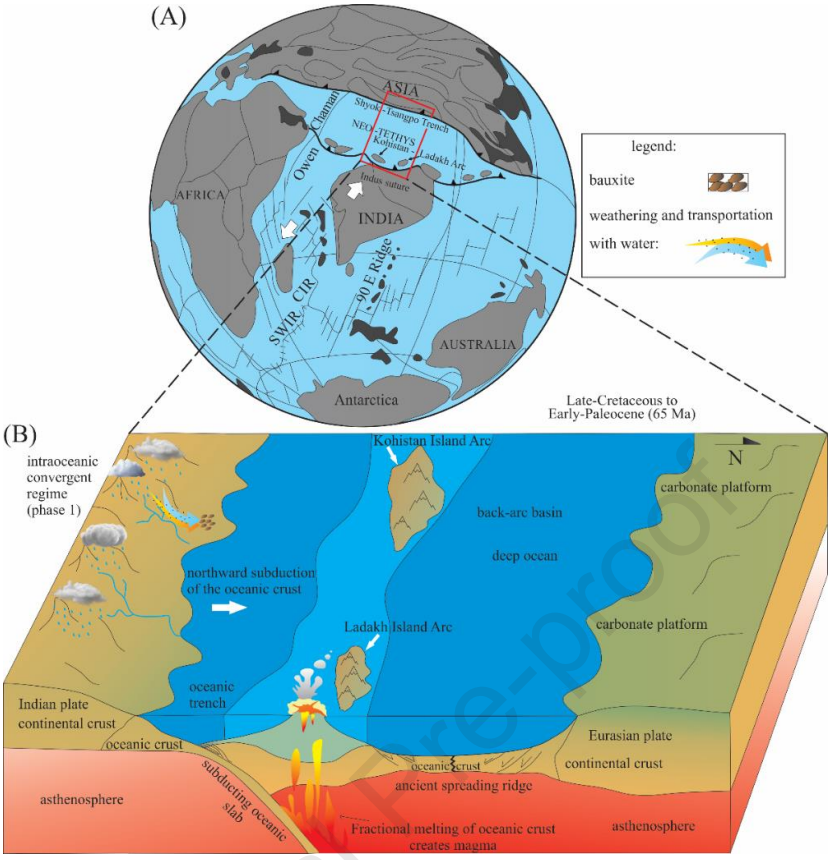

Fig. 15. (A) Regional tectonism from the Late Cretaceous to the Middle Paleocene around the Tethys Ocean (modified after (Chatterjee and Bajpai, 2016). The red square shows Fig. 15B. (B) Tectonic model showing intra-oceanic subduction of the Indo-Eurasian plates, related processes, and the sedimentary environment at the initial time of the deposition of the Hangu Formation (modified after (Yang et al., 2019).

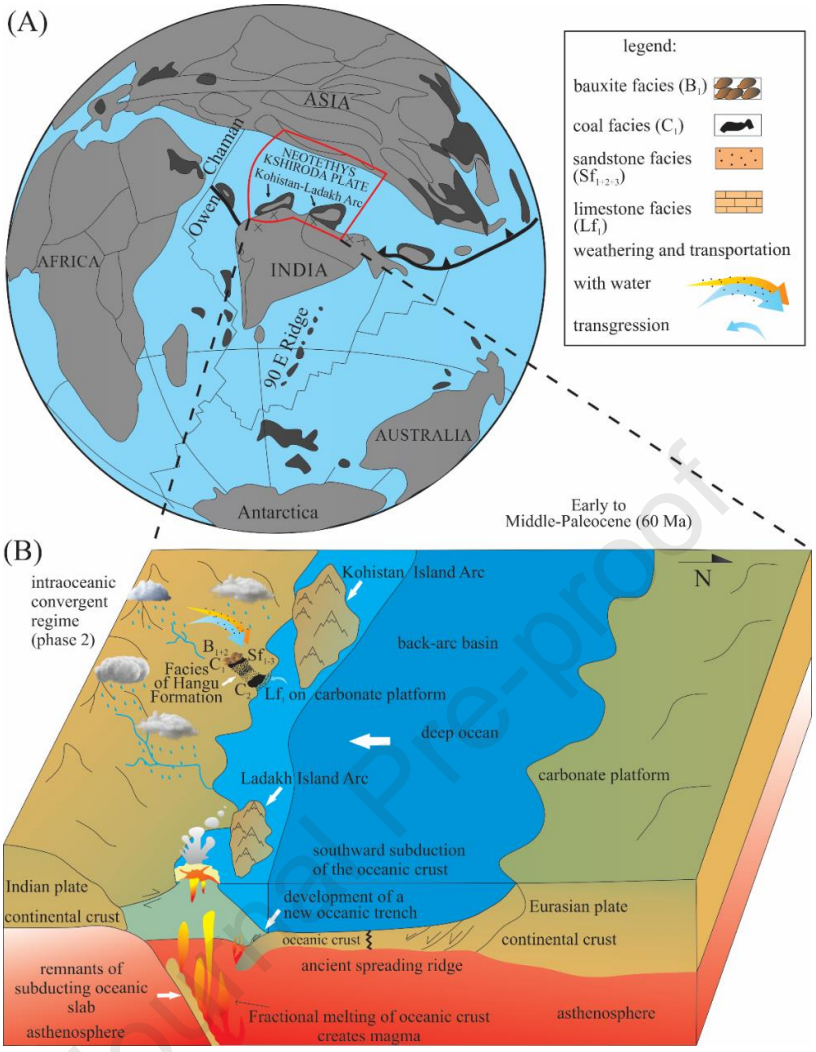

Fig. 16. (A) Regional tectonism from early to middle Paleocene around the Tethys Ocean (modified after (Chatterjee and Bajpai, 2016). The red square shows Fig. 15B. (B) Tectonic model showing the collision phase of the Indian continental plate and the KIA and its relationship with the climatic conditions and the sedimentary environment during the time of the deposition of Hangu Formations' facies suit (modified after (Yang et al., 2019).

Highlights

* An integrated petrological and sedimentological study has been carried out on the Hangu Formation

* Lithofacies and microfacies approach used for the better understanding of the paleoclimate and sedimentary environment

* Insight of paleoclimate was implemented to reconfirm the sedimentary environment

* Integration of sedimentary environment, paleoclimate and facie shift is used to reconstruct the paleotectonic evolution

Declaration of interests

☒ The authors declare that they have no known competing financial interests or personal relationships that could have appeared to influence the work reported in this paper.

☐ The authors declare the following financial interests/personal relationships which may be considered as potential competing interests: